Cellular sources and targets of type I interferons that drive susceptibility to tuberculosis

Dmitri I. Kotov[1,2]*, Ophelia V. Lee[1], Charlotte Langner[1], Jaresley V. Guillen[1], Joshua M. Peters[3,4], Andres Moon[5], Eileen M. Burd[5], Kristen C. Witt[1], Daniel B. Stetson[6], David L. Jaye[5], Bryan D. Bryson[3,4], Russell E. Vance[1,2]*

[1]Divison of Immunology and Molecular Medicine, [2]Howard Hughes Medical Institute, University of California, Berkeley; [3]Department of Biological Engineering, MIT; [4]Ragon Institute of MGH, MIT, and Harvard; [5]Department of Pathology and Laboratory Medicine, Emory University, Atlanta; [6]Department of Immunology, University of Washington, Seattle
*Correspondence: dkotov@berkeley.edu, rvance@berkeley.edu

Summary

Mycobacterium tuberculosis (*Mtb*) causes 1.5 million deaths annually. Active tuberculosis correlates with a neutrophil-driven type I interferon (IFN) signature, but the cellular mechanisms underlying tuberculosis pathogenesis remain poorly understood. We found interstitial macrophages (IMs) and plasmacytoid dendritic cells (pDCs) are dominant producers of type I IFN during *Mtb* infection in mice and non-human primates, and pDCs localize near human *Mtb* granulomas. Depletion of pDCs reduces *Mtb* burdens, implicating pDCs in tuberculosis pathogenesis. During IFN-driven disease, we observe abundant DNA-containing neutrophil extracellular traps (NETs) known to activate pDCs. Single cell RNA-seq reveals type I IFNs act on IMs to impair their responses to IFNγ, a cytokine critical for *Mtb* control. Cell type-specific disruption of the type I IFN receptor suggests IFNs act on IMs to inhibit *Mtb* control. We propose pDC-derived type I IFNs, driven by NETs, act on IMs to drive bacterial replication, further neutrophil recruitment, and active tuberculosis disease.

Introduction

Mycobacterium tuberculosis (*Mtb*), the causative agent of tuberculosis disease, caused 1.5 million deaths in 2020[1]. Treatment requires a minimum 4-6 month course of antibiotics, or up to 2 years for increasingly prevalent multi-drug resistant strains. Moreover, the only approved vaccine for *Mtb* has variable or no efficacy in adults[2]. The pathophysiology of tuberculosis remains poorly understood. The mouse model has been essential to identify most of the host factors known to control tuberculosis in humans, including tumor necrosis factor and interferon-γ[3–5]. Nevertheless, the use of mice has been criticized for poorly recapitulating key aspects of human disease[6].

In humans, active tuberculosis disease is associated with the induction of anti-viral type I interferons (IFNs)[7–10]. A causal role for type I IFNs in driving human tuberculosis is supported by the finding that a partial loss-of-function mutation in type I IFN receptor (IFNAR) is associated with *Mtb* resistance in humans[11]. Conversely, infection with type I IFN inducing viruses is associated with worse *Mtb* infection outcomes in humans. For example, influenza infection correlates with an increased risk of death among patients with pulmonary tuberculosis, and infants with cytomegalovirus have an increased risk of tuberculosis disease[12–14]. A type I IFN response has the potential to be a driver of progression to active *Mtb* in humans, as type I IFNs can antagonize the critical, protective IFNγ response during mycobacterial infection[5,15,16]. Nevertheless, a causal and mechanistic link between type I IFNs and tuberculosis disease are extremely difficult to establish in human or non-human primate studies.

Mice are able to model the viral induced loss of *Mtb* control seen in humans, with chronic lymphocytic choriomeningitis virus (LCMV), acute LCMV, pneumonia virus of mice, and influenza A virus co-infection with *Mtb* all exacerbating tuberculosis disease[17–20]. Additionally,

virus-induced type I IFN drove the loss of *Mtb* control during the acute LCMV and influenza co-infections[17,18]. However, co-infection studies make it challenging to understand the cellular mechanism behind *Mtb* susceptibility, as perturbations such as type I IFN receptor blockade simultaneously impact viral and bacterial control. Therefore, an ideal platform for studying how type I IFN induces loss of *Mtb* control would be mice in which *Mtb* infection is sufficient to induce a hyper type I IFN response. However, C57BL/6 (B6) mice, the most used model for *Mtb* infection, generate a weak type I IFN response in response to *Mtb* infection without overt manipulation such as intranasal administration of poly I:C[9,21,22]. Indeed, IFNAR deletion from unmanipulated B6 mice does not impact bacterial burdens in the lungs[23–25]. Therefore, it has been challenging to decipher the cellular mechanism behind type I IFN production during *Mtb* infection and the effect of type I IFN on bacterial control.

Unlike B6 mice, C3H and 129 mice exhibit a type I interferon driven susceptibility to *Mtb*[26], but there are limited genetic tools in these mouse strains, making mechanistic studies difficult. We have recently discovered that congenic B6 mice with the 'super susceptibility to tuberculosis 1' region from C3H mice (B6.*Sst1*^{S}) [27,28] are highly susceptible to *Mtb* infection due to their strong type I IFN response. IFNAR deletion fully rescues the susceptibility of B6.*Sst1*^{S} mice at early timepoints and enhances survival[29]. We recently identified *Sp140* as the gene responsible for the *Sst1*^{S} phenotype and confirmed that the early *Mtb* susceptibility of *Sp140*$^{-/-}$ mice is also rescued by IFNAR deletion[30]. As *Sp140*$^{-/-}$ mice were generated on a pure C57BL/6J background, this mouse model allows for mechanistic studies of the type I IFN response during *Mtb* infection.

In the present study, we leveraged *Sp140*$^{-/-}$ mice to identify the cellular mechanisms by which type I IFN drives *Mtb* susceptibility. Single cell RNA-sequencing (scRNA-seq) identified interstitial macrophages (IMs) as a major type I IFN producer. A sensitive genetic reporter of type I IFN production corroborated the scRNA-seq findings, and also revealed that plasmacytoid dendritic cells (pDCs) are an additional source of type I IFN during *Mtb* infection. Type I IFN production by pDCs appears to drive disease since pDC depletion rescued the susceptibility of *Sp140*$^{-/-}$ mice. Type I IFN conferred susceptibility by acting on IMs, dampening their ability to respond to IFNγ[16,31,32]. Loss of bacterial control in *Sp140*$^{-/-}$ mice leads to an influx of neutrophils and abundant production of DNA-rich neutrophil extracellular traps (NETs), ligands known to promote type I IFN production by pDCs[33,34]. Our findings suggest a new model of tuberculosis pathogenesis in which type I IFNs impair responses to IFNγ to drive an initial loss of bacterial control, which in turn initiates a positive feedback loop of NET production and type I IFN expression by pDCs, leading to uncontrolled bacterial replication and active tuberculosis disease.

Results

Myeloid cells harbor Mtb in Sp140$^{-/-}$ *mice*

As we have previously demonstrated, the susceptibility of *Sp140*$^{-/-}$ mice to *Mtb* infection is driven by type I IFN, and mirrors the correlation between type I IFN and active tuberculosis disease seen in humans. Genetic or antibody-mediated depletion of IFNAR fully rescues the enhanced susceptibility of *Sp140*$^{-/-}$ animals (**Fig. 1A**)[30]. To better characterize the immune response of *Sp140*$^{-/-}$ mice to *Mtb*, we infected mice with *Mtb* harboring a Wasabi fluorescent protein expression plasmid[35], which permits robust detection of *Mtb*-infected cells by flow cytometry. With this approach, we were able to clearly identify *Mtb*-harboring cells in mouse lungs 25 days post-infection (**Fig. 1B**). The vast majority of the bacteria isolated from these lungs were highly fluorescent, indicating that the plasmid is stably maintained for at least 25 days. The number of *Mtb* infected cells detected by flow cytometry strongly correlates with lung *Mtb* CFU (R^2 = 0.6281), indicating that flow cytometry reliably reports the cellular distribution of

Mtb 25 days post-infection (**Fig. 1C**). We classified lung immune cells as CD11b$^+$ Ly6G$^+$ neutrophils, CD64$^+$ MerTK$^+$ Siglec F$^+$ alveolar macrophages (AMs), CD64$^+$ MerTK$^+$ Siglec F$^-$ CD11b$^+$ IMs, or CD64$^+$ MerTK$^-$ CD11b$^+$ monocytes and assessed the abundance of these cells at day 25 after *Mtb* infection in *Sp140*$^{-/-}$ and *Sp140*$^{-/-}$ *Ifnar1*$^{-/-}$ mice (**Supplementary Fig. 1**). The lungs of infected *Sp140*$^{-/-}$ animals contained significantly more neutrophils, IMs, and monocytes as compared to *Sp140*$^{-/-}$ *Ifnar1*$^{-/-}$ mice, with no difference in the number of AMs (**Fig. 1D**). Over 90% of the infected cells were myeloid cells (**Fig. 1B, 1E**), in line with previous reports[36,37]. Consistent with their higher abundance in infected *Sp140*$^{-/-}$ lungs, neutrophils comprised a considerably larger percentage and absolute number of the *Mtb* infected cells in *Sp140*$^{-/-}$ mice compared to *Sp140*$^{-/-}$ *Ifnar1*$^{-/-}$ animals (**Fig. 1E, 1F**). There were also more infected IMs and monocytes in *Sp140*$^{-/-}$ mice compared to *Sp140*$^{-/-}$ *Ifnar1*$^{-/-}$ animals, in line with the overall increase in these immune populations in the lungs of infected *Sp140*$^{-/-}$ mice (**Fig. 1D, 1F**). Importantly, we did not observe alterations in the immune compartment of uninfected *Sp140*$^{-/-}$ mice, implying grossly normal hematopoietic development in these mice (**Supplemental Fig. 2**)[38–40]. However, the exact mechanisms causing the infection-induced differences in myeloid cells from *Sp140*$^{-/-}$ mice was unclear, and thus required more in-depth profiling of the myeloid compartment.

Macrophages and Neutrophils exhibit a variety of activation states during Mtb infection

To further characterize the *Mtb*-infected myeloid cells and dissect the cellular mechanism of type I IFN driven *Mtb* susceptibility, we compared B6 and *Sp140*$^{-/-}$ innate immune responses by performing scRNA-seq on myeloid cells from *Mtb* infected or uninfected lungs 25 days after infection. For this experiment, CD64$^+$ and Ly6G$^+$ cells were magnetically enriched, sort purified, and processed for library generation with the 10X Genomics platform. To ensure proper cell clustering, mRNA transcripts and protein expression for select lineage markers were simultaneously measured by CITE-seq (**Supplementary Fig. 3**)[41]. Resulting datasets were analyzed with Seurat V4, and Weighted Nearest Neighbor (WNN) analysis was used to cluster cells based on mRNA and protein expression[42]. Analyzed datasets were then visualized by uniform manifold approximation and projection (UMAP) reduction on the WNN clustered data (wnnUMAP)[43]. The resulting dataset consists of 6,604 B6 and 13,668 *Sp140*$^{-/-}$ cells, almost exclusively consisting of myeloid cells (**Fig. 2A**). Major cell types were annotated based on protein or mRNA expression of lineage defining markers, such as Siglec F protein expression for identifying AMs (**Fig. 2B**)[44]. Individual clusters within a major cell type, like the 10 clusters of neutrophils, were annotated based on expression of maturation and activation markers (**Supplementary Fig. 4**). Each cluster is represented in the B6 and *Sp140*$^{-/-}$ datasets, however the proportions of some clusters, including the ratio of IFN stimulated gene (ISG)$^+$ IM to ISG$^-$ IM, shifts between genotypes (**Fig. 2C**). The largest changes in composition are seen when comparing cells from naïve lungs to bystander and *Mtb* infected cells from *Mtb* infected lungs (**Fig. 2D**). For example, AMs are abundant in naïve lungs but are rare among the *Mtb* infected cells 25 days post-infection, as also seen by flow cytometry **(Fig. 1F, 2D**). To establish whether the differences in immune response between *Sp140*$^{-/-}$ and B6 mice occurred in response to *Mtb* infection, we compared naïve *Sp140*$^{-/-}$ and B6 lungs by scRNA-seq. Consistent with the normal cellular profile of naïve *Sp140*$^{-/-}$ mice (**Supplementary Fig. 2**), fewer than 10 differentially expressed genes were identified between the two genotypes in AMs, IMs, monocytes, and neutrophils (**Supplementary Fig. 5**). These results suggest that the immune compartment of B6 and *Sp140*$^{-/-}$ mice is highly similar at baseline, and the type I IFN-driven changes in the genotypes occur after *Mtb* infection.

Bystander IMs and pDCs are the primary sources of type I IFN during Mtb infection

To determine the cellular mechanism of type I IFN-driven *Mtb* susceptibility, we first sought to identify which cells produce type I IFN following infection. In general, our scRNAseq analysis revealed that very few cells were *Ifnb1* positive, which may reflect a lack of sensitivity of scRNAseq, and/or the transient and stochastic expression pattern of this gene (**Fig. 3A**)[45–48]. *Mtb* induced expression of *Ifnb1* in infected and bystander mononuclear phagocytes, with a slight bias towards *Ifnb1* production by IMs compared to monocytes, and no production by AMs (**Fig. 3A**). While there was no major difference in the cell types producing *Ifnb1* between B6 and *Sp140*$^{-/-}$ cells, a greater number and frequency of *Sp140*$^{-/-}$ cells expressed *Ifnb1* compared to B6 cells (**Fig. 3B**). Additionally, *Ifnb1* expressing cells in *Sp140*$^{-/-}$ mice had higher per cell expression of *Ifnb1* than B6 cells (**Fig. 3C**). Consistent with these findings, a prior scRNA-seq study of *Mtb* infected and naïve lungs from non-human primates largely mirrors our findings in mice[49]. IMs were also the dominant *IFNB1*-expressing cells in non-human primates with active tuberculosis, and IMs did not express *IFNB1* in naïve or latently infected lungs (**Fig. 3D**). These results suggest that mice accurately model the *Mtb* induced type I IFN production seen in non-human primates.

The type I IFN producers identified in the scRNA-seq datasets were validated using a genetic reporter of type I IFN production, called I-Tomcat mice (from Dan Stetson, manuscript in preparation). These mice express TdTomato and Cre downstream of *Ifnb1*; therefore, any cell that expresses *Ifnb1* will also express TdTomato and Cre (**Fig. 3E**). While TdTomato expression was sufficient to identify *Ifnb1* expression by I-Tomcat bone marrow-derived macrophages following *in vitro* stimulation with poly I:C (**Supplementary Fig. 6**), TdTomato^{+} cells were not detected 25 days after *Mtb* infection (**Fig. 3F**). Even though type I IFN drives the *Mtb* susceptibility of *Sp140*$^{-/-}$ mice 25 days post-infection, it is unclear when the type I IFN production occurs (**Fig. 1A**). It is possible that type I IFN is an early and/or transient event, which would be missed by analyzing a single timepoint with the I-Tomcat mice. To address this issue, we crossed I-Tomcat mice with the Ai6 Cre reporter mouse line to generate I-Tomcat Ai6 mice (**Fig. 3E**)[50]. In these mice, any cell that has ever expressed *Ifnb1* will constitutively express ZsGreen. *Mtb* infected I-Tomcat Ai6 mice clearly contained populations of reporter-positive myeloid cells, while demonstrating low background among cell populations that are not expected to be reporter positive (e.g., ~0.1% of T cells were Ai6^{+}) (**Fig. 3G**). Consistent with the scRNAseq analysis, IMs and monocytes were the primary *Ifnb1* expressing cells in B6 and *Sp140*$^{-/-}$ mice (**Fig. 3H**). Interestingly, *Sp140*-deficient mice exhibited elevated Ai6^{+} expression frequency in all cell types, suggesting SP140 broadly modulates the sensitivity for inducing *Ifnb1* expression (**Fig. 3H**). In addition to corroborating the scRNA-seq data, the I-Tomcat mice also identified pDCs as a major type I IFN producing cell population. Lung pDCs are very rare and were therefore not represented in our scRNA-seq dataset, demonstrating the power of using genetic reporters to study rare events and cell populations. Despite their scarcity, pDCs are known to be extremely robust producers of type I IFNs on a per cell basis[51].

While we expected IMs to be a major type I IFN producing population given the scRNA-seq results, we were surprised that the majority of the Ai6^{+} IMs were *Mtb*$^{-}$ and most *Mtb*$^{+}$ IMs were Ai6^{-} (**Fig. 3G**). These results suggest that direct infection of IMs is neither required nor sufficient for IFN-β production. To examine this phenomenon in greater detail, we performed confocal microscopy and histo-cytometry analysis of *Mtb*-infected I-Tomcat Ai6 and *Sp140*$^{-/-}$ I-Tomcat Ai6 lungs[52,53]. While lesions of diseased tissue were clearly identifiable in I-Tomcat Ai6 mice, the size and myeloid cell influx into the diseased tissue were greatly exacerbated in *Sp140*$^{-/-}$ I-Tomcat Ai6 (**Fig. 4A**). Additionally, Ai6 expressing cells were identifiable throughout the lungs, with an increased propensity to localize in diseased rather than healthy tissue (**Fig. 4A, Supplementary Fig. 7**). Within diseased tissue, Ai6 expressing cells were primarily located near *Mtb* harboring cells in I-Tomcat Ai6 and *Sp140*$^{-/-}$ I-Tomcat Ai6 lungs (**Fig. 4B**). Similar to the flow cytometry results, SIRP□$^{+}$ macrophages were a major Ai6 expressing cell population, with a higher frequency of SIRP□$^{+}$ macrophages expressing Ai6 than CD4^{+} T cells in the

diseased tissue but not healthy tissue (**Fig. 3H, 4B, 4C**). Direct infection by *Mtb* was not a major driver of IFN-β expression, as ~2-3% of infected macrophages were Ai6^{+} and ~12-15% of Ai6^{+} cells were *Mtb* infected, in line with the frequencies seen in IMs by flow cytometry (**Fig. 3H, 4D**). These results suggest that IM localization to *Mtb* rich regions provides the activating signals required for IFN-β expression, while direct infection of IMs is not required for IFN-β expression.

pDCs significantly contribute to the Mtb susceptibility of Sp140$^{-/-}$ animals

While pDCs have a well-established role in anti-viral immunity in the lung, limited work has assessed their contribution during *Mtb* infection[54,55]. pDCs may have been previously overlooked because of their scarcity in the lung. Despite this scarcity, pDCs can have major effects due to the extremely high levels of interferons produced per cell[51]. Consistent with our finding that pDCs are a major type I IFN producer in *Mtb* infected mouse lungs, Khader and colleagues described the presence of pDCs in lungs of non-human primates with active pulmonary TB[49]. However, the lack of genetic tools in non-human primates precluded functional studies of pDCs during TB. Therefore, we decided to take advantage of our experimentally tractable mouse model to assess whether pDCs affect *Mtb* control. The contribution of pDCs was initially tested by depleting pDCs using an anti-PDCA-1 antibody[56–58]. This strategy efficiently depleted pDCs and resulted in a partial rescue of *Mtb* control in *Sp140$^{-/-}$* mice (**Fig. 5A, 5B**). However, PDCA-1 is known to be upregulated by cells other than pDCs in inflammatory environments, thus antibody depletion could have been protective against *Mtb* by depleting non-pDC cells[57]. We therefore also tested the contribution of pDCs by using a genetic pDC depletion strategy in which we generated *Sp140$^{-/-}$* mice with diphtheria toxin receptor (DTR) expressed downstream of the human BDCA2 promoter (pDC-DTR)[59]. As a single copy of *Sp140* is sufficient to restore wild-type control of *Mtb*, the *Sp140$^{+/-}$* littermate controls are representative of wild-type, *Mtb* restrictive animals. DT administration efficiently ablated pDCs in *Sp140$^{-/-}$* and *Sp140$^{+/-}$* mice, with the depletion specifically affecting pDCs (**Fig. 5C**, **Supplementary Fig. 8**). Genetic pDC depletion was able to fully rescue bacterial control in *Sp140$^{-/-}$* mice, while depletion in *Sp140*-sufficient animals (that do not exhibit an exacerbated type I IFN response) did not affect lung bacterial burden, as expected (**Fig. 5D**). These results demonstrate a novel contribution by pDCs in limiting *Mtb* control in animals with a hyper type I IFN response.

To understand why pDCs contribute to the susceptibility of *Sp140$^{-/-}$* but not *Sp140*-sufficient animals, we examined ligand availability for the pDCs. We focused on DNA-rich NETs as a potential pDC-activating ligand because extracellular DNA is a potent pDC-activating ligand, and NETs have been described as a stimulus for type I interferon production by pDCs in mice and humans in the context of autoimmunity[33,34,60]. Additionally, another *Mtb* susceptible mouse model with a hyper type I interferon response identified the presence of NETs in the lungs of susceptible mice and humans with active *Mtb* disease[61]. We assessed NET production in *Sp140$^{-/-}$* and B6 mice by staining for citrullinated H3 in the lungs of *Mtb* infected mice (**Fig. 5E**). *Sp140$^{-/-}$* mice had over a 100-fold increase in NET staining as compared to B6 animals, indicating that *Sp140$^{-/-}$* mice have substantially more ligand to activate type I interferon production by pDCs as compared to wild-type hosts (**Fig. 5F**).

While our results demonstrate a role for pDCs during *Mtb* infection in mice and the Khader lab identified a correlation between pDCs and active *Mtb* in non-human primates, the role of pDCs during human *Mtb* infection has yet to be examined[49]. Therefore, we analyzed human lung and lymph node biopsies taken from *Mtb* culture-positive patients for the presence of pDCs near *Mtb* granulomas (**Fig. 5G**). Based on CD303 and CD123 staining, pDCs localized to the lymphocytic cuff surrounding *Mtb* granulomas in human lungs and lymph nodes (**Fig. 5H**, **5I**, **Supplementary Fig. 8**). Of the 8 patient samples analyzed, 5 lung samples and 7 lymph node samples had pDCs in the same 400× field as an *Mtb* granuloma (**Supplementary Table**

1). The majority of the pDCs in the lung samples were distributed as individual cells, while lymph node pDCs were primarily grouped together in clusters of over 20 cells or scattered individually (**Supplementary Table 1**). These results demonstrate that pDCs, though generally an extremely rare cell population, are nevertheless located near *Mtb*-infected cells in granulomas in human lung and lymph nodes. These results, along with our results in mice and previous studies in non-human primates[49], implicate pDCs as a plausible source of type I IFN that drives active tuberculosis in humans.

Neutrophils and IMs are the major sensors of type I IFNs during Mtb infection

Having identified pDCs, IMs, and monocytes as the major type I IFN producers during *Mtb* infection, we next sought to identify which cells responded to this type I IFN. As expected, IFNAR was uniformly expressed by all lung myeloid cells, and therefore not informative for identifying IFN responsive cells (**Fig. 6A**)[62]. However, comparing differentially expressed genes in B6 and *Sp140*$^{-/-}$ neutrophils and IMs showed a clear induction of IFN stimulated genes in cells from *Sp140*$^{-/-}$ animals (**Fig. 6B**). A major complication, however, is that many genes induced by type I IFN are also induced by IFNγ, and most existing studies do not distinguish the two. Therefore, we sought to develop type I IFN-specific and IFNγ-specific transcriptional signatures. We analyzed RNA-sequencing on human macrophages stimulated with IFNγ, IFN-β, tumor necrosis factor, transforming growth factor-β, or nothing (**Supplementary Fig. 9**)[63]. After converting the gene names to mouse gene symbols, the signatures were applied to the mouse lung myeloid scRNA-seq dataset. Strength of signature expression in naïve mice was used to define the threshold for classifying cells as an IFNγ or type I IFN responder (**Supplementary Fig. 9**). As expected, naïve mice had very few cells responding to either cytokine, while bystander and *Mtb* infected cells responded strongly to type I and 2 IFNs (**Fig. 6C**). Interestingly, the type I IFN response was limited to IMs and neutrophils, even though monocytes and AMs were responsive to IFNγ. Potentially, differences in the localization of these cells could explain their differences in cytokine responsiveness. As expected, neutrophils and IMs from *Sp140*$^{-/-}$ mice exhibited a significant increase in type I IFN signaling relative to cells from B6 lungs (**Fig. 6D, 6E**). Consistent with considerable prior work demonstrating that type I IFNs impair responsiveness to IFNγ[16,31,32,64], the *Sp140*$^{-/-}$ mice harbored a distinct population of IMs that exhibited the signature of type I IFN-responsiveness but lacked the signature of IFNγ responsiveness (note the distinct population of blue IMs in **Fig. 6D, 6E**). Since IFNγ is critical for control of intracellular *Mtb* replication, these results suggest that type I IFN inhibits *Mtb* control at least in part by opening a niche of susceptible IMs that fail to respond to IFNγ.

As neutrophils and IMs were the primary sensors of type I IFN, these are the cell types we tested to determine which cell population mediates the type I IFN-driven susceptibility of *Sp140*$^{-/-}$ mice. Using LysM^{Cre} *Ifnar1*$^{fl/fl}$ mice, we deleted IFNAR expression on myeloid cells in *Sp140*$^{-/-}$ mice. Myeloid cell-specific deficiency in IFNAR was sufficient to rescue bacterial control and reduce lung neutrophil numbers to the same extent as global IFNAR deletion (**Fig. 7A, 7B**). As LysM^{cre} is activate in neutrophils, monocytes, and macrophages, this strategy could not dissociate the contribution of type I IFN signaling in neutrophils from that in mononuclear phagocytes. Therefore, we isolated the contribution of neutrophil sensing of type I IFN by deleting IFNAR solely on neutrophils by using Mrp8^{Cre} *Ifnar1*$^{fl/fl}$ mice. Neutrophil-specific deficiency in type I IFN signaling was insufficient to rescue the *Mtb* susceptibility or the increase in lung neutrophils exhibited by *Sp140*$^{-/-}$ mice (**Fig. 7C, 7D**). Taken together, these results are consistent with a model in which type I IFNs act on IMs to inhibit IFNγ signaling in these cells, thereby reducing their ability to restrict *Mtb* growth.

Discussion

The dominant gene signature identified in humans with active tuberculosis disease is a type I IFN signature. Type I IFNs are a critical for effective anti-viral immunity[8] but considerable data from humans and animal models indicate type I IFNs impair *Mtb* control[7,9,10,65]. Interestingly, not all IFNs promote *Mtb* disease, as IFNγ (also called type II IFN) is protective during tuberculosis[5]. Indeed, type I IFNs can exacerbate bacterial infections by directly antagonizing IFNγ signaling. The mechanism of antagonism is poorly understood but seems to be due at least in part to the downregulation of surface expression of the IFNγ receptor[31,32]. The antagonism of IFNγ signaling by type I IFNs is conserved in humans, and has been shown to be relevant during *Mycobacterium leprae* infections[16]. Potentially, antagonism of IFNγ signaling underlies the tuberculosis-susceptibility of humans that exhibit a type I IFN signature, as humans with active *Mtb* exhibit reduced IFNγ receptor expression on their monocytes[15]. Additionally, type I IFNs can antagonize IL-1 signaling, an additional pathway that is also critical for *Mtb* control, through the induction of IL-1 receptor antagonist and eicosanoid imbalance[22,29,66,67]. Thus, the type I interferon response may be a key driver of progression to active tuberculosis. There is support in the literature for this hypothesis, as infants in their first year of life that acquire cytomegalovirus infection, a virus known to induce type I IFN, have a high risk of developing tuberculosis disease[12,13,68–70]. Additionally, influenza infection, which also induces type I IFN, correlates with an increased risk of death in pulmonary tuberculosis patients[14]. While the correlation between viral infection and exacerbated tuberculosis disease is tantalizing, a major limitation of studying human disease is the difficulty in establishing the underlying causal mechanisms that account for the correlation. Thus, we turned to a mouse model of *Mtb* infection to establish the cellular mechanisms by which type I IFN drives *Mtb* susceptibility.

The commonly used B6 mouse model does not exhibit a strong type I IFN response after *Mtb* infection. Consistent with the modest type I IFN response of B6 mice, IFNAR deletion on the B6 genetic background does not impact survival or bacterial burdens in the lungs after *Mtb* infection[23–25,29]. Therefore, we sought a different mouse model that recapitulated two key aspects of human disease, the hyper type I IFN response and the accompanying neutrophilic inflammation[7,71,72]. Previously, we identified B6.*Sst1*^{S} mice as a mouse model that exhibits type I IFN-driven susceptibility to *Mtb* infection[29]. We then defined *Sp140* as the gene responsible for the susceptibility of these mice[30]. As was the case for B6.*Sst1*^{S} animals, IFNAR deletion in *Sp140*$^{-/-}$ mice rescues susceptibility. Additionally, *Sp140*$^{-/-}$ mice have more lung neutrophils after *Mtb* infection than *Sp140*$^{-/-}$ *Ifnar1*$^{-/-}$ animals (**Fig. 1D, 7B, 7D**). Therefore, *Sp140*$^{-/-}$ mice recapitulate the fundamental type I IFN and neutrophilic character of human active *Mtb* disease, and can serve as a platform for understanding the cellular mechanism of type I IFN-driven *Mtb* susceptibility.

Sp140$^{-/-}$ mice provide a unique model of the aberrant type I IFN response, as they do not require repeated administration of TLR agonists, viral co-infection, or other perturbations of the innate immune system for type I IFN production[17,18,21,22,61]. Other groups have also modeled the type I IFN response by infecting B6 mice with a lineage 2 clinical *Mtb* strain, such as HN878[73,74]. However, IFNAR deletion had no impact on survival or bacterial control at early time points in B6 mice infected with HN878, unlike *Sp140*$^{-/-}$ mice infected with *Mtb* Erdman[30,75,76]. Thus, we believe the *Sp140*$^{-/-}$ mouse model uniquely recapitulates the hyper type I IFN response exhibited by humans, and provides a tool to study the mechanistic basis of the aberrant type I IFN response.

We sought to use the *Sp140*$^{-/-}$ mice to address two key questions: (1) what cells produce type I IFN-producing during *Mtb* infection? and (2) which cells respond to the type I IFN to mediate *Mtb* disease? Flow cytometry and imaging of I-Tomcat Ai6 *Ifnb1* reporter mice identified IMs and pDCs as the major IFN-β producers during *Mtb* infection. Imaging provided insight into why these cells expressed type I IFN, as the frequency of type I IFN-expressing

macrophages was enriched relative to CD4$^+$ T cells in diseased tissue but not in healthy tissue. This result suggests that proximity to *Mtb* dictates access to activating signals required to induce IFN-β expression by macrophages. However, most IFN-β expressing IMs were not infected with *Mtb*, and most infected IMs were not *Ifnb1* or reporter positive, indicating direct infection is insufficient and may not be the main driver of type I IFN expression *in vivo*. Imaging demonstrated that B6 and *Sp140*$^{-/-}$ macrophages expressed IFN-β at similar frequencies in diseased tissue. This result appears to contrast with flow cytometry analysis of whole lungs, which demonstrates a higher frequency of IMs expressing IFN-β in *Sp140*$^{-/-}$ mice relative to B6 mice. The apparent discrepancy between the flow cytometry and imaging data is likely explained by the fact that *Sp140*$^{-/-}$ mice have considerably more diseased tissue than B6 mice. Additionally, the Ai6 signal from I-Tomcat Ai6 mice identifies cells that have expressed IFN-β, but does not indicate the level of IFN-β expression in these cells. Thus, even if macrophages are driven to express IFN-β at similar frequencies in B6 and *Sp140*$^{-/-}$ mice, the macrophages in *Sp140*$^{-/-}$ mice could produce more IFN-β per cell, as seen in the scRNA-seq data (**Fig. 3C**).

Expression of type I IFNs by pDCs during *Mtb* infection was particularly noteworthy as limited work exists on the effect of pDCs on *Mtb* control. The role of pDCs in viral control is well established, with considerable evidence that pDC production of type I IFN during the early phases of viral infections significantly contributes to viral control[54,55,59]. In bacteria, the potential for pDCs to impact control has become appreciated more recently, with pDCs demonstrating a protective function against *Citrobacter rodentium*, *Chlamydia pneumoniae*, and *Klebsiella pneumoniae*[77–80]. However, few studies have examined the contribution of pDCs during *Mtb* infection, and these studies have not yet led to a clear understanding. The number of pDCs in the blood was reduced in *Mtb* infected humans, but lung pDC numbers or function were not assessed[81,82]. In non-human primates, there was a correlation between active pulmonary *Mtb* and the influx of pDCs and IFN-responsive macrophages into the lungs of the rhesus macaques[49]. Another group also identified pDCs in tuberculosis granulomas of a different non-human primate, cynomolgus macaques, but the frequency of pDCs among all cells in the granulomas did not correlate with bacterial burden of the granuloma[83]. A major issue in the studies using NHPs or humans is the difficulty in depleting or otherwise functionally assessing the role of pDCs. We therefore generated *Sp140*$^{-/-}$ pDC-DTR mice to study the contribution of pDCs to bacterial control. These mice permit specific depletion of pDCs during *Mtb* infection and demonstrated that pDCs contribute significantly to the susceptibility of *Sp140*$^{-/-}$ mice. Additionally, we identified pDCs in the lymphocytic cuff surrounding *Mtb* granulomas in human lungs and lymph nodes. Together, these results suggest that disease progression driven by pDC production of type I IFN drives disease in mice, and is likely conserved across non-human primates and humans.

While pDC depletion rescued *Sp140*$^{-/-}$ mice, it had no impact on the bacterial burdens in B6 animals. This result was not surprising given that very few myeloid cells in B6 mice expressed a type I IFN signature and *Ifnar1* deficiency also has only modest effects in the B6 background[25,29]. As pDCs are present in B6 and *Sp140*$^{-/-}$ mice, we speculated that the difference in pDC type I IFN production in these mouse strains could be due in part to differences in the availability of activating ligands. As seen in another *Mtb* susceptible mouse model, and in *Mtb* infected human lungs[61], *Sp140*$^{-/-}$ mice had a significant enrichment in NET production compared to B6 mice. Potentially, these NETs, which are DNA-rich products of neutrophils, act as ligands for TLR9 on the pDCs, as described in mouse and human autoimmunity[33,34,60,84]. Given that NET formation was also identified in *Mtb* granulomas in human lung sections, it is possible that pDC sensing of NETs contributes to the type I IFN response detected in humans with active *Mtb* disease[61].

Having defined the cells producing type I IFNs *in vivo* after *Mtb* infection, we then sought to identify which cells responded to the type I IFN. To do this, we had to first develop transcriptional signatures that distinguish the response to type I IFN from the closely related

response to IFNγ. Applying these signatures to our scRNA-seq data, we identified neutrophils and IMs as type I IFN sensors. While both cell populations harbor *Mtb*, it is possible that type I IFN driven susceptibility to *Mtb* is caused by signaling in only one of these populations. In a GM-CSF blockade model of type I IFN driven *Mtb* susceptibility, neutrophil-specific deletion of IFNAR rescued bacterial control[61]. We employed the same genetic strategy as this prior report, but were unable to detect any rescue of *Sp140*$^{-/-}$ mice when neutrophils lacked IFNAR. This was surprising as we saw that *Sp140*$^{-/-}$ neutrophils expressed a type I IFN gene signature by scRNA-seq. However, GM-CSF is critical for maintaining lung alveolar macrophages and the responsiveness of lung monocytes and macrophages to infections, including *Mtb* infection[85–88]. Therefore, it is possible that impairing lung macrophages by GM-CSF blockade shifted the impact of type I IFN on *Mtb* control from macrophages to neutrophils. In support of this idea, we also identified IMs as a type I IFN-sensing population, and deletion of IFNAR on macrophages rescued *Sp140*$^{-/-}$ mouse bacterial control. These results suggest that during a normal (GM-CSF sufficient) response, type I IFN signaling in macrophages reduces their ability to restrict *Mtb* in a cell-intrinsic manner, potentially by inhibiting IFNγ signaling in the macrophages[15,31,32].

Overall, our results suggest a model in which type I IFNs impair responsiveness to IFNγ, leading to an initial loss of bacterial control. Bacterial replication then leads to neutrophil influx and NET production within the diseased tissue. We propose that DNA-rich NETs are sensed by pDCs, likely via TLR9, causing them to produce type I IFN, which further antagonizes IFNγ signaling and reduces the IMs ability to restrict *Mtb* growth. Given the correlations between our results and findings in rhesus macaques and humans with active *Mtb*, we believe that our proposed mechanism of type I IFN driven loss of *Mtb* control is conserved across species. These findings open the door for the development of therapies targeting NET production or pDC function as host-directed strategies for treating *Mtb* infection.

Acknowledgments

We thank members of the Vance, Barton, Stanley, and Cox laboratories for advice and discussions; M. Colonna for advice on pDC depletion; B. Malissen, Y. Belkaid, and A. Lacy-Hulbert for mouse lines; P. Dietzen, R. Chavez, and J. Morales for technical assistance; A. Valeros, H. Nolla, and K. Heydari of the UC Berkeley Cancer Research Laboratory Flow Cytometry facility for assistance with flow cytometry; H. Aaron and F. Ives of the UC Berkeley Cancer Research Laboratory Molecular Imaging Center (RRID:SCR_017852) for assistance with confocal microscopy (supported by the Helen Wills Neuroscience Institute). D.I.K. was supported by an NIH Postdoctoral Fellowship (F32HL158250). R.E.V. is an Investigator of the Howard Hughes Medical Institute and is funded by NIH grants AI075039, AI063302 and AI155634.

Author Contributions

Conceptualization: D.I.K. and R.E.V. Investigation: D.I.K., O.V.L., C.L., J.M.P., A.M., and E.B. Data analysis: D.I.K. Methodology: J.G., K.C.W., and D.B.S. Resources: D.B.S. Writing: D.I.K. and R.E.V. with input from all co-authors. Funding acquisition: R.E.V. Supervision: R.E.V., D.B.S., D.L.J., and B.D.B.

Declaration of Interests

R.E.V. consults for Ventus Therapeutics and Tempest Therapeutics.

Figure Legends

Figure 1. Myeloid cells are the dominant *Mtb* harboring cells in *Sp140*$^{-/-}$ and *Sp140*$^{-/-}$ *Ifnar1*$^{-/-}$ mice. (**A**) Colony forming units of *Mtb* in the lungs of *Sp140*$^{-/-}$ (n = 13) and *Sp140*$^{-/-}$ *Ifnar1*$^{-/-}$ (n = 11) mice 25 days post-infection. (**B**) Representative flow cytometry plots of an *Mtb*-infected *Sp140*$^{-/-}$ mouse lung gated on live CD45^{+} B220^{-} CD90.2^{-} cells to identify *Mtb* infected cells, subset into neutrophils (green; Ly6G^{+} CD11b^{+}), other cells (purple; Ly6G^{-} CD64^{-} MerTK^{-}), monocytes (blue; Ly6G^{-} CD64^{+} MerTK^{low}), alveolar macrophages (AMs; orange; Ly6G^{-} CD64^{+} MerTK^{high} Siglec F^{+}), and interstitial macrophages (IMs; pink; Ly6G^{-} CD64^{+} MerTK^{high} Siglec F^{-}). (**C**) Correlation between the number of infected cells identified by flow cytometry of total lung digests gated as in Fig. 1B to the colony forming units from the same infected lung (*Sp140*$^{-/-}$ and *Sp140*$^{-/-}$ *Ifnar1*$^{-/-}$ combined; n = 45). The red line indicates a nonlinear regression of the displayed data. (**D**) Number of innate immune cells by cell type in the lungs of *Mtb*-infected *Sp140*$^{-/-}$ (n = 19; closed circles) and *Sp140*$^{-/-}$ *Ifnar1*$^{-/-}$ mice (n = 16; open circles). (**E**) Frequency and (**F**) number by immune cell population of *Mtb*-infected cells in *Sp140*$^{-/-}$ (n = 12-19; closed circles) and *Sp140*$^{-/-}$ *Ifnar1*$^{-/-}$ mice (n = 10-15; open circles). Lungs were analyzed for the depicted experiments 24-26 days after *Mtb* infection. The bars in (A), (D), (E), and (F) represent the median. Pooled data from two or three independent experiments are shown. A linear regression performed on log transformed data was used to calculate significance and R^2 for (C). An unpaired t test was used to determine significance for (A), a two-way ANOVA with Sidak's multiple comparisons test was used to calculate significance for (D), (E), and (F). **p < 0.01, ***p < 0.001, ****p < 0.0001.

Figure 2. ScRNA-sequencing analysis of B6 and *Sp140*$^{-/-}$ myeloid cells from *Mtb* infected and naïve lungs. CITE-seq was used to perform scRNA-sequencing analysis to integrate transcriptomic and protein expression of single cells, as described further in Supplementary Fig. 3. (**A**) Weighted nearest neighbor UMAP plot depicting unbiased clustering of myeloid cells combining all cells from wild-type B6 and *Sp140*$^{-/-}$ *Mtb*-infected and naïve lungs (n = 10 lungs; n= 20272 cells). (**B**) Dot plot of lineage defining protein and mRNA markers used to annotate the dataset. (**C**) Weighted nearest neighbor UMAP plot comparing cells from B6 and *Sp140*$^{-/-}$ lungs. (**D**) Weighted nearest neighbor UMAP plot contrasting cells from naïve mice, the bystander cells from *Mtb*-infected mice, and the *Mtb*-infected cells from *Mtb*-infected mice (B6 and *Sp140*$^{-/-}$ combined). Lungs were analyzed for the depicted experiment 25 days after *Mtb*-Wasabi infection. For each genotype, n = 3 for the infected lung samples and n = 2 for the naïve lung samples. *p < 0.05, **p < 0.01.

Figure 3. Interstitial macrophages, monocytes, and plasmacytoid dendritic cells are the primary IFN-β producers in mice and non-human primates. (**A**) Weighted nearest neighbor UMAP plot of *Ifnb1* expression in myeloid cells from naïve mice, bystander myeloid cells from infected mice, and *Mtb* infected myeloid cells from infected mice (B6 and *Sp140*$^{-/-}$ combined). (**B**) Weighted nearest neighbor UMAP plot of *Ifnb1* expression in myeloid cells from B6 and *Sp140*$^{-/-}$ mice. (**C**) Violin plot depicting level of *Ifnb1* expression in B6 and *Sp140*$^{-/-}$ cells that express *Ifnb1*. (**D**) Analysis of GSE149758 scRNA-seq data from Esaulova E., *et al*. 2021. UMAP depicting *IFNB1* expression in cells from non-human primates with active *Mtb* infection, latent *Mtb* infection, or that are uninfected. (**E**) Schematic representation of the genetic structure of I-Tomcat mice and Ai6 mice. Cre expression permanently deletes the loxP-flanked STOP cassette resulting in constitutive ZsGreen expression. (**F**) Representative flow cytometry plot indicating lack of detectable TdTomato expression in immune cells. (**G**) Representative flow

cytometry plots of ZsGreen expression and *Mtb*-mCherry detection in T cells, IMs, pDCs, and monocytes. (**H**) Frequency of Ai6 expressing cells in lung immune cells from Ai6^{-} control (n = 34; open circles), *Sp140*$^{-/-}$ I-Tomcat Ai6 (n = 19; green circles), and I-Tomcat Ai6 (n = 15; red circles) mice. The bars in (H) represent the median. Pooled data from four independent experiments are shown in (H). Lungs were analyzed for the depicted experiments 25 days after *Mtb* infection. Statistical significance in (H) was calculated by one-way ANOVA with Tukey's multiple comparison test. *p < 0.05, **p < 0.01, ***p < 0.001, ****p < 0.0001.

Figure 4. Cells producing IFN-β are enriched in diseased tissue, but only a minority harbor *Mtb*. (**A**) Representative images of *Mtb*-infected I-Tomcat Ai6 and *Sp140*$^{-/-}$ I-Tomcat Ai6 lung sections stained for SIRP□ (dark blue), CD4 (yellow), B220 (teal), Ly6G (red), Ai6 (green), and *Mtb*-expressed mCherry (magenta). Inset images depict higher magnification of diseased and healthy tissue for both genotypes. (**B**) Representative images of Ai6^{+} cell localization near *Mtb* in the diseased portions of I-Tomcat Ai6 and *Sp140*$^{-/-}$ I-Tomcat Ai6 lungs. Sections were stained with SIRP□ (dark blue), CD4 (yellow), Ai6 (green), and *Mtb*-expressed mCherry (magenta). White arrows indicate cells co-expressing Ai6 and SIRP□. (**C**) Image quantification of the frequency of Ai6 expression in CD4^{+} T cells and SIRP□$^{+}$ IMs in the diseased and healthy tissue of B6 I-Tomcat Ai6 (n = 5) and *Sp140*$^{-/-}$ I-Tomcat Ai6 (n = 7) lungs. (**D**) Image quantification of the frequency of Ai6 expression among *Mtb*-infected macrophages or frequency of *Mtb* infection among Ai6^{+} cells for B6 I-Tomcat Ai6 (n = 5) and *Sp140*$^{-/-}$ I-Tomcat Ai6 (n = 7) lungs. All samples were analyzed 25 days after *Mtb* infection. Pooled data from two independent experiments are shown in (C) and (D). Statistical significance in (C) and (D) was calculated with an unpaired t test. ***p < 0.001.

Figure 5. pDC depletion reduces *Mtb* burdens in *Sp140*$^{-/-}$ mice, and pDCs are present in the lymphocytic cuff surrounding granulomas in *Mtb*-infected human lymph nodes and lungs. (**A**) Number of splenic pDCs and (**B**) bacterial burden in *Sp140*$^{-/-}$ mice that received isotype or pDC depleting antibody from days 12 to 24 post-infection (n = 9-12). (**C**) Number of splenic pDCs and (**D**) bacterial burden in *Sp140*$^{-/-}$ pDC-DTR mice or *Sp140*$^{-/-}$ mice controls that received DT from days 12 to 24 after infection (n = 10-13). (**E**) Representative images and (**F**) quantification of NET production based on citrullinated H3 staining in the diseased portions of I-Tomcat Ai6 and *Sp140*$^{-/-}$ I-Tomcat Ai6 lungs. Sections were stained with citrullinated H3 (red), Ai6 (green), Ly6G (teal), and *Mtb*-expressed mCherry (magenta) (n = 6-7). (**G**) Representative hematoxylin and eosin or (**H**) anti-CD303 (brown) and hematoxylin staining on serial sections of *Mtb*-infected human lymph nodes (n = 8). (**I**) Representative hematoxylin and eosin and anti-CD303 (brown) and hematoxylin staining on serial sections of *Mtb*-infected human lung samples (n = 8). Mouse lungs were harvested 25 days post-infection. The bars in (A), (B), (C), (D), and (F) represent the median. Pooled data from two independent experiments are shown in (A), (B), (C), (D), and (F). Statistical significance was calculated by one-way ANOVA with Tukey's multiple comparison test for (B), (C), and (D) and by an unpaired t test for (A) and (F). **p < 0.01, ***p < 0.001, ****p < 0.0001.

Figure 6. Neutrophils and IMs in *Mtb*-infected *Sp140*$^{-/-}$ lungs respond to type I IFNs and exhibit impaired responses to IFNγ. (**A**) Weighted nearest neighbor UMAP plot of *Ifnar1* and *Ifnar2* mRNA expression in innate immune cells from *Mtb*-infected lungs (B6 and *Sp140*$^{-/-}$ combined). (**B**) Volcano plot of differentially expressed genes comparing B6 and *Sp140*$^{-/-}$ neutrophils and IMs, with higher log fold change indicating greater expression in B6. (**C**) Weighted nearest neighbor UMAP plot of naïve, bystander, and *Mtb*-infected lung myeloid cells (B6 and *Sp140*$^{-/-}$ combined) classified by their responsiveness to IFNγ (red), type I IFN (blue), both (purple), or neither (grey). Signatures are defined in Supplementary Fig. 9A. (**D**) Weighted nearest neighbor UMAP plot and (**E**) graph of the frequency of neutrophils, monocytes, IMs, and

AMs from bystander and *Mtb*-infected B6 (n = 3) and *Sp140*$^{-/-}$ (n = 3) lungs that are responsive to IFNγ (red), type I IFN (blue), both (purple), or neither (white). Lungs were analyzed 25 days after *Mtb*-Wasabi infection. Statistical significance in (B) was calculated with the Wilcoxon Rank-Sum test and by two-way ANOVA with Tukey's multiple comparisons test in (E). *p < 0.05, ***p < 0.001, ****p < 0.0001.

Figure 7. Macrophage recognition of type I IFN drives the *Mtb* susceptibility of *Sp140*$^{-/-}$ mice. (**A**) Colony forming units and (**B**) number of neutrophils in the lungs of *Sp140*$^{-/-}$ *Ifnar1*$^{-/-}$ (n = 11), *Sp140*$^{-/-}$ *Ifnar1*$^{fl/fl}$ LysM^{cre} (n = 18), and *Sp140*$^{-/-}$ littermate control (n = 34) mice 24-25 days after *Mtb* infection. (**C**) Bacterial burdens and (**D**) neutrophil numbers in the lungs of *Sp140*$^{-/-}$ *Ifnar1*$^{-/-}$ (n = 11-16), *Sp140*$^{-/-}$ *Ifnar1*$^{fl/fl}$ Mrp8^{cre} (n = 10-18), and *Sp140*$^{-/-}$ littermate control (n = 28-57) mice. The bars in (A), (B), (C), and (D) represent the median. Lungs were analyzed for the depicted experiments 24-26 days after *Mtb* infection. Pooled data from two-three independent experiments are shown. Statistical significance was calculated by one-way ANOVA with Tukey's multiple comparison test. *p < 0.05, **p < 0.01, ***p < 0.001, ****p < 0.0001.

Materials and Methods

Mice

Mice were maintained under specific pathogen-free conditions and housed at 23°C with a 12 hour light-dark cycle in accordance with the regulatory standards of the University of California Berkeley Institutional Animal Care and Use Committee. All mice were sex- and age-matched and were 6-12 weeks old at the start of infections. Male and female mice were used in all experiments. Littermate controls were used when possible, as indicated in the figure legends. B6, B6.129S2-Ifnar1^{tm1Agt}/Mmjax (*Ifnar1*$^{-/-}$)[89], B6.Cg-Gt(ROSA)26Sor$^{tm6(CAG-ZsGreen1)Hze}$/J (Ai6)[50], B6(Cg)-Ifnar1$^{tm1.1Ees}$/J (*Ifnar1*^{fl})[90], B6.Cg-Tg(S100A8-cre,-EGFP)1Ilw/J (Mrp8^{Cre})[91], and B6.129P2-Lyz2$^{tm1(cre)Ifo}$/J (LysM^{Cre})[92] mice were purchased from Jackson Laboratories. *Ifnb1*-Tomato-Cre-pA Terminator (I-Tomcat) mice were a gift from D. Stetson at the University of Washington and a manuscript describing these mice in detail is currently in preparation. B6-Fcgr1^{tm2Ciphe} (CD64^{Cre})[93] mice were a gift from B. Malissen at Centre d'Immunologie de Marseille Luminy and were provided by Y. Belkaid at the National Institutes of Health. B6-Tg(CLEC4C-HBEGF)956Cln/J (pDC-DTR)[59] mice were provided by A. Lacy-Hulbert at the Benaroya Research Institute. *Sp140*$^{-/-}$ mice were previously generated in-house[30]. *Sp140*$^{-/-}$ *Ifnar1*$^{-/-}$ mice were generated by crossing *Sp140*$^{-/-}$ mice with *Ifnar1*$^{-/-}$ mice in-house. I-Tomcat Ai6 mice were generated by crossing I-Tomcat mice with Ai6 mice, while *Sp140*$^{-/-}$ I-Tomcat Ai6 mice were the result of crossing I-Tomcat mice with *Sp140*$^{-/-}$ and Ai6 mice in-house. *Sp140*$^{-/-}$ mice were crossed in-house with pDC-DTR mice to generate *Sp140*$^{-/-}$ pDC-DTR mice. *Sp140*$^{-/-}$ *Ifnar1*^{fl} LysM^{cre}, *Sp140*$^{-/-}$ *Ifnar1*^{fl} Mrp8^{Cre}, and *Sp140*$^{-/-}$ *Ifnar1*^{fl} CD64^{Cre} mice were generated by crossing *Sp140*$^{-/-}$ mice with *Ifnar1*^{fl} and LysM^{Cre} or Mrp8^{Cre} or CD64^{Cre} mice in-house.

Mtb infections

Mtb strain Erdman was a gift of S. A. Stanley. Frozen aliquoted stocks were produced after passing the strain *in vivo* to ensure virulence. *Mtb* expressing Wasabi (*Mtb*-Wasabi) and *Mtb*-mCherry were generated using *Mtb* that had been passaged 2 or fewer times *in vitro*. For these fluorescent strains, *Mtb* was grown in Middlebrook 7H9 liquid medium supplemented with 10% albumin-dextrose-saline, 0.4% glycerol, and 0.05% Tween-80 for 5 days at 37°C. The cells were pelleted and washed in 10% glycerol to remove salt. The bacteria were then electroporated with

1 µg DNA using a 2 mm electroporation cuvette and the following settings: 2500 volts, 1000 Ohms, 25 µF. The pTEC15 plasmid (a gift from Lalita Ramakrishnan; Addgene plasmid # 30174), which expresses Wasabi under the control of the Mycobacterium Strong Promoter, was electroporated into *Mtb* to generate *Mtb*-Wasabi[35]. The pMSP12::mCherry plasmid (a gift from Lalita Ramakrishnan; Addgene plasmid # 30167), which expresses mCherry under the control of the Mycobacterium Strong Promoter, was electroporated into *Mtb* to generate *Mtb*-mCherry. Following electroporation, bacteria were grown on 7H11 plates supplemented with 10% oleic acid, albumin, dextrose, and catalase, 0.5% glycerol, and either 200 µg / mL Hygromycin for *Mtb*-Wasabi or 50 µg / mL Kanamycin for *Mtb*-mCherry for 3-4 weeks at 37°C. Individual colonies where then propagated in 10 mL inkwell flask cultures using 7H9 medium supplemented with 10% albumin-dextrose-saline, 0.4% glycerol, 0.05% Tween-80, and either Hygromycin for *Mtb*-Wasabi or Kanamycin for *Mtb*-mCherry for 7 days at 37°C. The inkwell cultures were expanded into a 100 mL culture using the same 7H9 supplemented media with antibiotics and cultured for 4-5 days at 37°C. Once the bacteria were in log phase, the culture was filtered with a 5 µm syringe filter and frozen in 1 mL aliquots in 10% glycerol. For infection, a frozen aliquot was diluted in distilled H_20, and 9 mL of diluted culture was loaded into the nebulizer of a inhalation exposure system (Glas-Col, Terre Haute, IN) to deliver ~20-100 bacteria per mouse as determined by measuring CFU in lungs 1 day post-infection.

Tissue Processing for CFU and Flow cytometry

Mice were harvested at various days post-infection (as described in figure legends) to measure CFUs by plating and innate immune populations by flow cytometry. All lung lobes were harvested into a gentleMACS C tube (Miltenyi Biotec) containing 3 mL of RPMI media with 70 µg / mL of Liberase TM (Roche) and 30 µg / mL of Dnase I (Roche). Samples were processed into chunks using the lung_01 setting on the gentleMACS (Miltenyi Biotec) and incubated for 30 minutes at 37°C. Tissue was then homogenized into a single cell suspension by running the samples on the lung_02 setting on the gentleMACS. The digestion was quenched by adding 2 mL of PBS with 20% Newborn Calf Serum (Thermo Fisher Scientific) and filtered through 70 µm SmartStrainers (Miltenyi Biotec).

For measuring plasmacytoid dendritic cell numbers, spleens were harvested into a 12 well plate with 1 mL of PBS with 2% Newborn Calf Serum and 0.05% sodium azide in each well. The spleens were sandwiched between 100 uM mesh filters and mashed into a single cell suspension with the back of a syringe plunger. The single cell suspensions were filtered through 70 µm SmartStrainers (Miltenyi Biotec).

Measuring Bacterial Burden

To measure CFU, 50 µL was taken from each single cell suspension and then serially diluted in phosphate-buffered saline (PBS) with 0.05% Tween-80. Serial dilutions were plated on 7H11 plates supplemented with 10% oleic acid, albumin, dextrose, and catalase and 0.5% glycerol. Colonies were counted after 3 weeks.

Flow Cytometry

For flow cytometry, lung single cell suspensions were pelleted and resuspended in 500 µL of PBS with 2% Newborn Calf Serum and 0.05% Sodium azide and 100-150 µL were stained with antibodies for analysis. Spleen single cell suspensions were pelleted and resuspended in 5 mL of PBS with 2% Newborn Calf Serum and 0.05% Sodium azide, of which 50 µL were stained with antibodies. Single cell suspensions were stained for 45 minutes to an hour at room temperature with the following antibodies: TruStain FcX PLUS (S17011E, BioLegend), BUV496-

labeled CD45 (30-F11, BD Biosciences), APC-labeled CD64 (X54-5/7.1, BioLegend), BV480-labeled B220 (RA3-6B2, BD Biosciences), BV480-labeled CD90.2 (53-2.1, BD Biosciences), APC-Fire 750-labeled Ly6G (1A8, BioLegend), BUV395-labeled CD11b (M1/70, BD Biosciences), BUV737-labeled CD11c (HL3, BD Biosciences), APC-R700-labeled Siglec F (E50-2440, BD Biosciences), PE-labeled MerTK (DS5MMER, Thermo Fisher Scientific), Super Bright 645-labeled MHC II (M5/114.15.2, Thermo Fisher Scientific), BV421-labeled PD-L1 (MIH5, BD Biosciences), BV711-labeled Ly6C (HK1.4 , BioLegend), PE-labeled IFNAR-1 (MAR1-5A3, BioLegend), PE-Cy7-labeled MerTK (DS5MMER, Thermo Fisher Scientific), APC-eFluor 780-labeled CD11b (M1/70, Thermo Fisher Scientific), BUV395-labeled CCRL2 (BZ2E3, BD Biosciences), BUV563-labeled Ly6G (1A8, BD Biosciences), Percp-Cy5.5-labeled B220 (RA3-6B2, BioLegend), BV421-labeled Siglec H (440c, BD Biosciences), BV480-labeled CD19 (1D3, BD Biosciences), BV605-labeled MHC II (M5/114.15.2, BioLegend), BV785-labeled Ly6C (HK1.4 , BioLegend), BV605-labeled CD4 (GK1.5, BioLegend), BUV805-labeled CD8 (53-6.7, BD Biosciences), and PE-Cy7-labeled PDCA-1 (eBio927, Thermo Fisher Scientific). All samples also received fixable viability dye (Ghost Dye Violet 510; Tonbo Biosciences), Super Bright Complete Staining Buffer (Thermo Fisher Scientific), and True-Stain Monocyte Blocker (BioLegend) at the same time as the antibodies. Stained samples were fixed with cytofix/cytoperm (BD biosciences) for 20 minutes at room temperature before samples were removed from the BSL3. For intracellular staining, the fixed samples were stained with the following antibodies: PE-Cy7-labeled CD63 (NVG-2, BioLegend), Percp-eFluor 710-labeled iNOS (CXNFT, Thermo Fisher Scientific), BV785-labeled CD206 (C068C2, BioLegend). Cell numbers were calculated by adding fluorescent AccuCheck Counting Beads (Invitrogen) to each sample. Cells were then analyzed on a Fortessa (BD Biosciences) or an Aurora (Cytek) flow cytometer. Data were analyzed with Flowjo version 10 (BD Biosciences).

pDC depletion

Injections for pDC depletions were started 12 days after *Mtb* infection and continued every other day until the mice were harvested 25 days post-infection. Antibody depletion of pDCs was performed by administering 200 µg of anti-CD317 (927, BioXCell) or rat IgG2b isotype control antibody (LTF-2, BioXCell) in 200 µL PBS via intraperitoneal injection[57]. Genetic depletion involved administering 100 ng diphtheria toxin (Millipore Sigma) in 100 µL PBS via intraperitoneal injection into *Sp140*$^{-/-}$ pDC-DTR mice and littermate controls[59].

Immunostaining human lymph nodes and lungs

Human lung and lymph node samples were acquired from the surgical pathology archives of Emory University Hospital with appropriate institutional approval. 8 lung samples and 8 lymph node samples were analyzed. Each sample had been previously culture verified for *Mycobacterium tuberculosis* infection. The samples were formalin-fixed and paraffin-embedded. Sections were cut and stained with anti-CD123 (6h6, Thermo Fisher Scientific), anti-CD303 (124B3.13, Dendritics), or hematoxylin and eosin[94,95]. Primary antibodies were detected by immunoperoxidase staining with the LSAB+ System and a standard DAB reaction following manufacturer's instructions (DakoCytomation). Sections were counterstained with hematoxlyin prior to mounting and microscopy. pDCs were assessed in multiple 400× fields for each section to calculate the frequency of samples containing pDCs and the clustering of pDCs within each sample, defined as either singe cells, loose clusters of 5-20 cells, or tight clusters of more than 20 cells.

Confocal microscopy

Confocal Microscopy was performed using a Zeiss LSM 880 laser scanning confocal microscope (Zeiss) equipped with two photomultiplier detectors, a 34-channel GaASP spectral detector system, and a 2-channel AiryScan detector as well as 405, 458, 488, 514, 561, 594, and 633 lasers. 20 µm paraformaldehyde fixed lung sections from *Mtb*-mCherry infected I-Tomcat Ai6 and *Sp140*$^{-/-}$ I-Tomcat Ai6 mice were stained at 4°C overnight with BV421-labeled SIRP (P84, BD Biosciences), Pacific Blue–labeled B220 (RA3-6B2, BioLegend), eF506-labeled CD4 (RM4-5, BioLegend), and AF647-labeled Ly6G (1A8, BioLegend). Sections detecting the presence of Neutrophil extracellular traps (NETs) were stained with BV421-labeled Ly6G (1A8, BioLegend) and rabbit polyclonal anti-citrullinated histone-H3 (citrulline R2, R8, R17; Abcam), stained with AF488 donkey anti-rabbit secondary (Poly4064, BioLegend). Stained sections were inspected with a 5× air objective to find representative lesions and distal sites and then imaged using a 63× oil immersion objective lens with a numerical aperture of 1.4. For each infected lung, one *Mtb*-heavy lesion image and one distal site image was taken consisting of 20 µm z-stacks acquired at a 1.5 µm step size. For representative NET images, 4×4 tiled images were captured without a z-stack. Additionally, the Zeiss LSM 880 microscope was used to image single color-stained Ultracomp eBeads Plus (Thermo Fisher Scientific) for generating a compensation matrix.

Image processing and histo-cytometry analysis

Image analysis was performed using Chrysalis software[53]. Briefly, a compensation matrix was generated by automatic image-based spectral measurements on single color-stained controls in ImageJ by using Generate Compensation Matrix script. This compensation matrix was used to perform linear unmixing on three-dimensional images with Chrysalis. Chrysalis was also used for further image processing, including rescaling data and generating new channels by performing mathematical operations using existing channels. For histo-cytometry analysis, Imaris 9.9.1 (Bitplane) was used for surface creation to digitally identify cells in images based on protein expression[52]. Statistics for the identified cells were exported from Imaris and then imported into FlowJo version 10 (BD Biosciences) for quantitative image analysis.

Sorting Immune Cells for scRNA-seq analysis

3 B6 and 3 *Sp140*$^{-/-}$ mice were infected with less than 100 CFU of *Mtb*-Wasabi bacteria. Lungs from infected animals as well as 2 naïve control mice per genotype were harvested 25 days post-infection and processed as described for CFU and flow cytometry analysis. Single cell suspensions were resuspended in PBS with 2% Newborn Calf Serum and stained with TruStain FcX PLUS (S17011E, BioLegend), APC-labeled Ly6G (1A8, BioLegend), APC-labeled CD64 (X54-5/7.1, BioLegend), and TotalSeq-A-labeled Ly6G (1A8, BioLegend) anti-mouse antibodies on ice for 30 minutes. Myeloid cells were then magnetically enriched using an EasySep APC Positive Selection Kit II (StemCell Technologies) and MojoSort Magnets (BioLegend). All enriched samples were stained with the following panel of TotalSeq-A-labeled anti-mouse antibodies to detect protein expression in the scRNA-seq dataset: Ly6C (HK1.4, BioLegend), CD44 (IM7, BioLegend), CD169 (3D6.112, BioLegend), CD274 (MIH6 , BioLegend), Siglec F (S17007L, BioLegend), CSF1R (AFS98, BioLegend), CD11b (M1/70, BioLegend), CD86 (GL-1, BioLegend), MHC II (M5/114.15.2, BioLegend), and CX3CR1 (SA011F11, BioLegend). All samples were also stained with a unique anti-mouse TotalSeq-A Hashtag antibody (1-6; BioLegend) to allow up to 6 populations to be multiplexed in a single lane on a 10X Genomics Chromium Next GEM Chip[96]. Enriched cells from infected mice were also stained with PE-labeled B220 (RA3-6B2, Tonbo), PE-labeled CD90.2 (30-H12, Tonbo), and BV785-labeled CD45.2 (104, BioLegend) anti-mouse antibodies. Enriched cells from naïve mice were stained with Pacific Blue-labeled B220 (RA3-6B2, BioLegend), Pacific Blue-labeled CD90.2 (53-2.1,

BioLegend), PE-labeled F4/80 (BM8, Thermo Fisher Scientific), and BV786-labeled CD45.2 (104, BioLegend) anti-mouse antibodies. All post-enrichment antibody staining was performed on ice for 45 minutes in the presence of True-Stain Monocyte Blocker (BioLegend). Following staining, cells were resuspended in PBS with 2% Newborn Calf Serum and Sytox Blue Dead Cell Stain (Thermo Fisher Scientific). Cells were sort purified using a 100 µm microfluidic sorting chip in a 4 laser SH-800 cell sorter (Sony) on the purity setting. The isolated populations from infected lungs were *Mtb*-infected cells and bystander myeloid cells. Macrophages and a mixture of neutrophils and monocytes were isolated from the naïve lungs and the macrophages were combined with neutrophil/monocyte mixture at a 1:2 ratio for better macrophage representation in the resulting dataset.

Single cell RNA: Library generation and sequencing.

The scRNA-sequencing libraries were generated using the v3.1 chemistry Chromium Single Cell 3' Reagent Kit (10X Genomics) largely following the manufacturer protocol with the following minor modifications. Cells were loaded into 3 different lanes on a Chromium Next GEM Chip. Lane 1 was loaded with *Mtb*-infected cells from all 3 B6 and 3 *Sp140*$^{-/-}$ lungs. Lane 2 was loaded with bystander myeloid cells from the 3 infected B6 lungs as well as the myeloid cell mixture from the 2 naïve B6 lungs. Lane 3 was loaded with bystander myeloid cells from the 3 infected *Sp140*$^{-/-}$ lungs as well as the myeloid cell mixture from the 2 naïve *Sp140*$^{-/-}$ lungs. All 3 lanes of the Chromium Next GEM Chip were super-loaded with 29000 cells with a target of 14800 single cells per lane, as hashtag barcoding allows for a lower effective multiplet rate due to the ability to identify most of the multiplets (https://satijalab.org/costpercell/)[96]. 0.5 U/µL RNaseOUT Recombinant Ribonuclease Inhibitor (Invitrogen) was added to single cell RT master mix during the loading step and 1 µL of ADT and HTO additive primers (0.2 µM stock) were added during the cDNA amplification, as recommended by the CITE-seq and Cell Hashing Protocol (https://cite-seq.com/protocols/)[41]. Following cDNA, ADT, and HTO purification, samples were decontaminated by 2 rounds of centrifugation through 0.2 µM filter microcentrifuge tubes and then removed from the BSL3. Library preparations were completed outside of the BSL3 following the 10X Genomics protocol for the cDNA and the CITE-seq and Cell Hashing Protocol for the ADT and HTO libraries. Quality control of the libraries was performed with a Fragment Analyzer (Agilent). The mRNA, ADT, and HTO libraries were pooled at the following proportions: 85% mRNA, 9% ADT, and 6% HTO. Libraries were sequenced on a NovaSeq 6000 (Illumina) using two lanes of a S1 flow cell and the following cycles read 1 (28 cycles), i7 index (10 cycles), i5 index (10 cycles), read 2 (90 cycles).

ScRNA-seq: data processing.

Raw sequencing reads for the mRNA libraries were processed into raw count matrices with CellRanger version 4.0.0 (10X Genomics). The ADT and HTO libraries were processed into raw count matrices with CITE-Seq-Count version 1.4.3 (https://hoohm.github.io/CITE-seq-Count/)[97]. The raw counts for mRNA, ADT, and HTO were analyzed using Seurat v4.1.1 using default settings for normalizing the data, finding variable features, and scaling the data[42]. HTO demultiplexing was performed with the HTODemux function. Data was filtered to only include single cells with between 200 and 4500 genes and less than 5% mitochondrial reads. The resulting datasets were integrated together using 30 dimensions for the FindIntegrationAnchors function and 30 dimensions for the IntegrateData function. The data was then scaled and analyzed by PCA with 30 principal components followed by UMAP analysis with 30 dimensions. Clustering was performed by using 30 dimensions with the FindNeighbors function and a resolution of 0.8 for the FindClusters function.

To improve resolution for clustering innate immune cells, weighted nearest neighbor analysis was used to combine the protein data (ADTs) and the mRNA data when clustering cells. For this analysis, variable ADT features were identified and then normalized using centered log ratio transformation and a margin of 2. The normalized ADT data was then scaled and analyzed by PCA. The ADT and mRNA data was then combined with the FindMultiModalNeighbors function using 30 dimensions for the mRNA and 10 for the protein. The resulting dataset was analyzed by UMAP and clusters were identified with the FindClusters function using algorithm 3 and a resolution of 1.5[43].

Type I IFN and IFNγ Gene Signature Analysis

For generating the type I IFN and IFNγ gene signatures, we utilized a published RNA-seq dataset (GEO: GSE20251) of primary human macrophages that were unstimulated or stimulated with 10 ng / mL of TNF, IFNγ, IFN-β, or transforming growth factor-β for 24 hours and then processed for RNA-sequencing[63]. Gene expression was compared across all stimulation conditions and filtered to only include genes that were differentially expressed by an adjusted p-value of less than 0.001. The list was also filtered to only include genes with a normalized average expression of greater than 2. A gene specificity index was calculated based on the ratio of expression of a gene within a stimulation group over the average expression across all groups. The list was further filtered to only include genes with a gene specificity index greater than 1.5. Gene names were then converted to mouse symbols and any genes that did not have a mouse homolog where removed. The gene signature for IFNγ and type I IFN were then generated by finding all genes uniquely induced by IFNγ or type I IFN, respectively, from the filtered gene list. The UCell R package was used to score cells in the scRNA-seq dataset for their expression of either gene signature[98].

Statistical analysis

Statistical significance was determined using Prism (GraphPad) software for unpaired two-tailed Student t test when comparing two populations, one-way or two-way ANOVA tests with Tukey's or Sidak's multiple comparisons test when comparing multiple groups. Prism (GraphPad) was also used to calculate linear correlations and R^2.

Data and code availability

Raw and processed single cell RNA-sequencing data is deposited at GEO: XXXXXX. Code for scRNA-sequencing analysis is available on Github: https://github.com/dmitrikotov/Sp140-Type-I-Inteferon.

Supplementary Figure Legends

Supplementary Figure 1. Representative flow cytometry gating strategy to identify innate immune cell populations in *Mtb*-infected lungs. (**A**) Gating strategy for identifying neutrophils, eosinophils, monocytes, dendritic cells (DCs), alveolar macrophages (AMs), interstitial macrophages (IMs), and *Mtb* infected cells. Very few *Mtb*$^+$ cells were detected among the lymphoid and non-hematopoietic-derived cells (**B**) Representative identification of activated (CD63$^+$ PD-L1$^+$ or iNOS$^+$) neutrophils and interstitial macrophages in tuberculosis infected lungs. (**C**) Histogram comparing CD11c and MHC II expression on AMs (orange), monocytes (blue), and IMs (red).

Supplementary Figure 2. Naïve *Sp140*$^{-/-}$ mice exhibit minimally altered immune cell numbers by flow cytometry. Comparison of innate and adaptive immune cell numbers between B6 (n = 7; closed circles) and *Sp140*$^{-/-}$ (n = 8; open circles) (**A**) spleen, (**B**) lung, (**C**) and thymus. The bars in (A), (B), and (C) represent the median. Pooled data from two independent experiments are shown in (A), (B), and (C). Statistical significance was calculated by multiple unpaired t tests in (A), (B), and (C).

Supplementary Figure 3. The scRNA-seq dataset is a CITE-seq experiment that represents multiple mice and combines mRNA and protein expression. (**A**) UMAP plots depicting cell clustering by mRNA expression, protein expression, or combined mRNA and protein expression (B6 and *Sp140*$^{-/-}$ combined). (**B**) Violin plot of the RNA weight of each cluster, thereby depicting clusters identified based primarily on mRNA (closer to RNA weight = 1) or protein (closer to RNA weight = 0; B6 and *Sp140*$^{-/-}$ combined). (**C**) Weighted nearest neighbor UMAP plot of the biological replicates from naïve and infected B6 and *Sp140*$^{-/-}$ mice. For each genotype, n = 3 for the infected lung samples and n = 2 for the naïve lung samples.

Supplementary Figure 4. The expression of protein and mRNA used to annotate the myeloid cell clusters in the scRNA-seq dataset. Markers used for annotating (**A**) neutrophil and (**B**) monocyte and macrophage clusters based on maturity, activation status, and unique gene expression. The data represents a total of 10 mice (n = 3 for the infected lung samples and n = 2 for the naïve lung samples from B6 and *Sp140*$^{-/-}$ mice).

Supplementary Figure 5. Naïve *Sp140*$^{-/-}$ mice do not exhibit increased inflammation by scRNA-seq. (**A**) Weighted nearest neighbor UMAP plot of myeloid cells from naïve lungs of B6 (n = 2) and *Sp140*$^{-/-}$ (n = 2) mice. (**B**) Volcano plot of the differentially expressed genes between B6 and *Sp140*$^{-/-}$ alveolar macrophages (AMs), interstitial macrophages (IMs), monocytes, and neutrophils. Greater fold change indicates higher expression in B6 relative to *Sp140*$^{-/-}$. Statistical significance in (B) was calculated with the Wilcoxon Rank-Sum test.

Supplementary Figure 6. I-Tomcat bone marrow-derived macrophages express TdTomato following poly I:C stimulation. (**A**) Representative flow cytometry plot of TdTomato expression by I-Tomcat bone marrow-derived macrophages that were unstimulated (grey) or stimulated with poly I:C (red line).

Supplementary Figure 7. Histo-cytometry image analysis of *Mtb*-infected I-Tomcat Ai6 mouse lungs. (**A**) Representative confocal microscopy image of SIRP□ (dark blue), CD4 (yellow), B220 (teal), Ly6G (red), Ai6 (green), and mCherry (magenta) staining in a section of mouse lung 25 days after *Mtb* infection. (**B**) Identifying cells within the image based on fluorescence intensity of individual channels as well as cellular morphology. (**C**) Flowjo analysis to quantify fluorescent signal intensity and distance to *Mtb* for cells identified in the image. (**D**) Representative Flowjo comparison of macrophages (red) and CD4^{+} T cells (blue) from an image of a diseased portion of an *Sp140*$^{-/-}$ lung. (**E**) Number of Ai6^{+} cells per 10^6 um^3 in diseased (closed circle) and healthy tissue (open circle) from B6 (n = 5) and *Sp140*$^{-/-}$ (n = 7) *Mtb*-infected mouse lungs. Mouse lungs were harvested 25 days after infection. Pooled data from two independent experiments are shown in (E). Statistical significance in (E) was calculated by multiple paired t tests. *$p < 0.05$.

Supplementary Figure 8. pDC-DTR mice specifically deplete pDCs without affecting major lung immune cell populations, and CD123 also identifies pDCs in *Mtb*-infected human lymph node samples. (**A**) Representative flow cytometry plot of splenic pDCs in

Sp140$^{+/-}$ pDC-DTR mice treated with PBS or DT from days 12 to 24 after *Mtb* infection. (**B**) Number of various immune cell populations in *Mtb*-infected lungs of *Sp140*$^{+/-}$ pDC-DTR (n = 13; filled circles) and *Sp140*$^{+/-}$ mice (n = 13; open circles). Mice received DT from days 12 to 24 post-infection. (**C**) anti-CD123 (brown) and hematoxylin staining on *Mtb*-infected human lymph nodes. Mouse lungs and spleens were harvested 25 days after infection. Pooled data from two independent experiments are shown in (B). The bars in (A), (B) represent the median. Statistical significance in (B) was calculated by multiple unpaired t tests. *$p < 0.05$.

Supplementary Figure 9. Generating gene signatures for identifying IFNγ and type I IFN responding cells. (**A**) List of genes used for the gene signature for IFNγ or type I IFN responsiveness. (**B**) Weighted nearest neighbor UMAP plot of the IFNγ and type I IFN gene signature expression on naïve, bystander, or *Mtb*-infected lung myeloid cells (B6 and *Sp140*$^{-/-}$ combined). (C) Weighted nearest neighbor UMAP plot comparing IFNγ and type I IFN gene signature expression on cells from B6 and *Sp140*$^{-/-}$ lungs.

Supplementary Tables

Supplementary Table 1

			pDC Distribution		
Tissue	**Cases**	**Cases with CD303^{+} cells (% total)**	**Groups of >20 cells (% total)**	**Groups of 5-20 cells (% total)**	**Single cells (% total)**
Lung	8	5 (63%)	0	1 (20%)	4 (80%)
Lymph node	8	7 (88%)	3 (43%)	1 (14%)	3 (43%)

Supplementary Table 1. Quantification of the number of human lung and lymph nodes with pDCs in the same field of view as *Mtb* granulomas, as well as enumeration of the pDC distribution.

References

1. WHO (2021). Global tuberculosis report 2021. https://www.who.int/publications-detail-redirect/9789240037021.

2. Katelaris, A.L., Jackson, C., Southern, J., Gupta, R.K., Drobniewski, F., Lalvani, A., Lipman, M., Mangtani, P., and Abubakar, I. (2020). Effectiveness of BCG Vaccination Against Mycobacterium tuberculosis Infection in Adults: A Cross-sectional Analysis of a UK-Based Cohort. J. Infect. Dis. *221*, 146–155. 10.1093/infdis/jiz430.

3. Cooper, A.M., Dalton, D.K., Stewart, T.A., Griffin, J.P., Russell, D.G., and Orme, I.M. (1993). Disseminated tuberculosis in interferon gamma gene-disrupted mice. J. Exp. Med. *178*, 2243–2247. 10.1084/jem.178.6.2243.

4. Flynn, J.L., Goldstein, M.M., Chan, J., Triebold, K.J., Pfeffer, K., Lowenstein, C.J., Schreiber, R., Mak, T.W., and Bloom, B.R. (1995). Tumor necrosis factor-alpha is required in the protective immune response against Mycobacterium tuberculosis in mice. Immunity *2*, 561–572. 10.1016/1074-7613(95)90001-2.

5. Flynn, J.L., Chan, J., Triebold, K.J., Dalton, D.K., Stewart, T.A., and Bloom, B.R. (1993). An essential role for interferon gamma in resistance to Mycobacterium tuberculosis infection. J. Exp. Med. *178*, 2249–2254. 10.1084/jem.178.6.2249.

6. Russell, D.G., Barry, C.E., and Flynn, J.L. (2010). Tuberculosis: what we don't know can, and does, hurt us. Science *328*, 852–856. 10.1126/science.1184784.

7. Berry, M.P.R., Graham, C.M., McNab, F.W., Xu, Z., Bloch, S.A.A., Oni, T., Wilkinson, K.A., Banchereau, R., Skinner, J., Wilkinson, R.J., et al. (2010). An interferon-inducible neutrophil-driven blood transcriptional signature in human tuberculosis. Nature *466*, 973–977. 10.1038/nature09247.

8. McNab, F., Mayer-Barber, K., Sher, A., Wack, A., and O'Garra, A. (2015). Type I interferons in infectious disease. Nat. Rev. Immunol. *15*, 87–103. 10.1038/nri3787.

9. Moreira-Teixeira, L., Mayer-Barber, K., Sher, A., and O'Garra, A. (2018). Type I interferons in tuberculosis: Foe and occasionally friend. J. Exp. Med. *215*, 1273–1285. 10.1084/jem.20180325.

10. Ottenhoff, T.H.M., Dass, R.H., Yang, N., Zhang, M.M., Wong, H.E.E., Sahiratmadja, E., Khor, C.C., Alisjahbana, B., Crevel, R. van, Marzuki, S., et al. (2012). Genome-Wide Expression Profiling Identifies Type 1 Interferon Response Pathways in Active Tuberculosis. PLOS ONE *7*, e45839. 10.1371/journal.pone.0045839.

11. Zhang, G., deWeerd, N.A., Stifter, S.A., Liu, L., Zhou, B., Wang, W., Zhou, Y., Ying, B., Hu, X., Matthews, A.Y., et al. (2018). A proline deletion in IFNAR1 impairs IFN-signaling and underlies increased resistance to tuberculosis in humans. Nat. Commun. *9*, 85. 10.1038/s41467-017-02611-z.

12. Martinez, L., Nicol, M.P., Wedderburn, C.J., Stadler, A., Botha, M., Workman, L., le Roux, D.M., and Zar, H.J. (2021). Cytomegalovirus acquisition in infancy and the risk of tuberculosis disease in childhood: a longitudinal birth cohort study in Cape Town, South Africa. Lancet Glob. Health *9*, e1740–e1749. 10.1016/S2214-109X(21)00407-1.

13. Müller, J., Tanner, R., Matsumiya, M., Snowden, M.A., Landry, B., Satti, I., Harris, S.A., O'Shea, M.K., Stockdale, L., Marsay, L., et al. (2019). Cytomegalovirus infection is a risk factor for tuberculosis disease in infants. JCI Insight *4*, 130090. 10.1172/jci.insight.130090.

14. Walaza, S., Tempia, S., Dawood, H., Variava, E., Moyes, J., Cohen, A.L., Wolter, N., Groome, M., von Mollendorf, C., Kahn, K., et al. (2015). Influenza virus infection is associated with increased risk of death amongst patients hospitalized with confirmed pulmonary tuberculosis in South Africa, 2010–2011. BMC Infect. Dis. *15*, 26. 10.1186/s12879-015-0746-x.

15. Singhal, A., Jaiswal, A., Arora, V.K., and Prasad, H.K. (2007). Modulation of Gamma Interferon Receptor 1 by Mycobacterium tuberculosis: a Potential Immune Response Evasive Mechanism. Infect. Immun. *75*, 2500–2510. 10.1128/IAI.01743-06.

16. Teles, R.M.B., Graeber, T.G., Krutzik, S.R., Montoya, D., Schenk, M., Lee, D.J., Komisopoulou, E., Kelly-Scumpia, K., Chun, R., Iyer, S.S., et al. (2013). Type I interferon suppresses type II interferon-triggered human anti-mycobacterial responses. Science *339*, 1448–1453. 10.1126/science.1233665.

17. Kang, T.G., Kwon, K.W., Kim, K., Lee, I., Kim, M.J., Ha, S.-J., and Shin, S.J. (2022). Viral coinfection promotes tuberculosis immunopathogenesis by type I IFN signaling-dependent impediment of Th1 cell pulmonary influx. Nat. Commun. *13*, 3155. 10.1038/s41467-022-30914-3.

18. Redford, P.S., Mayer-Barber, K.D., McNab, F.W., Stavropoulos, E., Wack, A., Sher, A., and O'Garra, A. (2014). Influenza A Virus Impairs Control of Mycobacterium tuberculosis Coinfection Through a Type I Interferon Receptor–Dependent Pathway. J. Infect. Dis. *209*, 270–274. 10.1093/infdis/jit424.

19. Volkert, M., Pierce, C., Horsfall, F.L., and Dubos, R.J. (1947). THE ENHANCING EFFECT OF CONCURRENT INFECTION WITH PNEUMOTROPIC VIRUSES ON PULMONARY TUBERCULOSIS IN MICE. J. Exp. Med. *86*, 203–214. 10.1084/jem.86.3.203.

20. Xu, W., Snell, L.M., Guo, M., Boukhaled, G., Macleod, B.L., Li, M., Tullius, M.V., Guidos, C.J., Tsao, M.-S., Divangahi, M., et al. (2021). Early innate and adaptive immune perturbations determine long-term severity of chronic virus and Mycobacterium tuberculosis coinfection. Immunity *54*, 526-541.e7. 10.1016/j.immuni.2021.01.003.

21. Antonelli, L.R.V., Gigliotti Rothfuchs, A., Gonçalves, R., Roffê, E., Cheever, A.W., Bafica, A., Salazar, A.M., Feng, C.G., and Sher, A. (2010). Intranasal Poly-IC treatment exacerbates tuberculosis in mice through the pulmonary recruitment of a pathogen-permissive monocyte/macrophage population. J. Clin. Invest. *120*, 1674–1682. 10.1172/JCI40817.

22. Mayer-Barber, K.D., Andrade, B.B., Oland, S.D., Amaral, E.P., Barber, D.L., Gonzales, J., Derrick, S.C., Shi, R., Kumar, N.P., Wei, W., et al. (2014). Host-directed therapy of tuberculosis based on interleukin-1 and type I interferon crosstalk. Nature *511*, 99–103. 10.1038/nature13489.

23. McNab, F.W., Ewbank, J., Rajsbaum, R., Stavropoulos, E., Martirosyan, A., Redford, P.S., Wu, X., Graham, C.M., Saraiva, M., Tsichlis, P., et al. (2013). TPL-2-ERK1/2 signaling promotes host resistance against intracellular bacterial infection by negative regulation of type I IFN production. J. Immunol. Baltim. Md 1950 *191*, 1732–1743. 10.4049/jimmunol.1300146.

24. Moreira-Teixeira, L., Redford, P.S., Stavropoulos, E., Ghilardi, N., Maynard, C.L., Weaver, C.T., Freitas do Rosário, A.P., Wu, X., Langhorne, J., and O'Garra, A. (2017). T Cell-Derived IL-10 Impairs Host Resistance to Mycobacterium tuberculosis Infection. J. Immunol. Baltim. Md 1950 *199*, 613–623. 10.4049/jimmunol.1601340.

25. Stanley, S.A., Johndrow, J.E., Manzanillo, P., and Cox, J.S. (2007). The Type I IFN response to infection with Mycobacterium tuberculosis requires ESX-1-mediated secretion and

contributes to pathogenesis. J. Immunol. Baltim. Md 1950 *178*, 3143–3152. 10.4049/jimmunol.178.5.3143.

26. Dorhoi, A., Yeremeev, V., Nouailles, G., Weiner, J., Jörg, S., Heinemann, E., Oberbeck-Müller, D., Knaul, J.K., Vogelzang, A., Reece, S.T., et al. (2014). Type I IFN signaling triggers immunopathology in tuberculosis-susceptible mice by modulating lung phagocyte dynamics. Eur. J. Immunol. *44*, 2380–2393. 10.1002/eji.201344219.

27. Pan, H., Yan, B.-S., Rojas, M., Shebzukhov, Y.V., Zhou, H., Kobzik, L., Higgins, D.E., Daly, M.J., Bloom, B.R., and Kramnik, I. (2005). Ipr1 gene mediates innate immunity to tuberculosis. Nature *434*, 767–772. 10.1038/nature03419.

28. Pichugin, A.V., Yan, B.-S., Sloutsky, A., Kobzik, L., and Kramnik, I. (2009). Dominant role of the sst1 locus in pathogenesis of necrotizing lung granulomas during chronic tuberculosis infection and reactivation in genetically resistant hosts. Am. J. Pathol. *174*, 2190–2201. 10.2353/ajpath.2009.081075.

29. Ji, D.X., Yamashiro, L.H., Chen, K.J., Mukaida, N., Kramnik, I., Darwin, K.H., and Vance, R.E. (2019). Type I interferon-driven susceptibility to Mycobacterium tuberculosis is mediated by IL-1Ra. Nat. Microbiol. *4*, 2128–2135. 10.1038/s41564-019-0578-3.

30. Ji, D.X., Witt, K.C., Kotov, D.I., Margolis, S.R., Louie, A., Chevée, V., Chen, K.J., Gaidt, M.M., Dhaliwal, H.S., Lee, A.Y., et al. (2021). Role of the transcriptional regulator SP140 in resistance to bacterial infections via repression of type I interferons. eLife *10*, e67290. 10.7554/eLife.67290.

31. Eshleman, E.M., Delgado, C., Kearney, S.J., Friedman, R.S., and Lenz, L.L. (2017). Down regulation of macrophage IFNGR1 exacerbates systemic L. monocytogenes infection. PLOS Pathog. *13*, e1006388. 10.1371/journal.ppat.1006388.

32. Rayamajhi, M., Humann, J., Penheiter, K., Andreasen, K., and Lenz, L.L. (2010). Induction of IFN-αβ enables Listeria monocytogenes to suppress macrophage activation by IFN-γ. J. Exp. Med. *207*, 327–337. 10.1084/jem.20091746.

33. Garcia-Romo, G.S., Caielli, S., Vega, B., Connolly, J., Allantaz, F., Xu, Z., Punaro, M., Baisch, J., Guiducci, C., Coffman, R.L., et al. (2011). Netting Neutrophils Are Major Inducers of Type I IFN Production in Pediatric Systemic Lupus Erythematosus. Sci. Transl. Med. *3*, 73ra20-73ra20. 10.1126/scitranslmed.3001201.

34. Lande, R., Ganguly, D., Facchinetti, V., Frasca, L., Conrad, C., Gregorio, J., Meller, S., Chamilos, G., Sebasigari, R., Riccieri, V., et al. (2011). Neutrophils Activate Plasmacytoid Dendritic Cells by Releasing Self-DNA–Peptide Complexes in Systemic Lupus Erythematosus. Sci. Transl. Med. *3*, 73ra19-73ra19. 10.1126/scitranslmed.3001180.

35. Takaki, K., Davis, J.M., Winglee, K., and Ramakrishnan, L. (2013). Evaluation of the pathogenesis and treatment of Mycobacterium marinum infection in zebrafish. Nat. Protoc. *8*, 1114–1124. 10.1038/nprot.2013.068.

36. Cohen, S.B., Gern, B.H., Delahaye, J.L., Adams, K.N., Plumlee, C.R., Winkler, J.K., Sherman, D.R., Gerner, M.Y., and Urdahl, K.B. (2018). Alveolar Macrophages Provide an Early Mycobacterium tuberculosis Niche and Initiate Dissemination. Cell Host Microbe *24*, 439-446.e4. 10.1016/j.chom.2018.08.001.

37. Huang, L., Nazarova, E.V., Tan, S., Liu, Y., and Russell, D.G. (2018). Growth of Mycobacterium tuberculosis in vivo segregates with host macrophage metabolism and ontogeny. J. Exp. Med. *215*, 1135–1152. 10.1084/jem.20172020.

38. Amatullah, H., Fraschilla, I., Digumarthi, S., Huang, J., Adiliaghdam, F., Bonilla, G., Wong, L.P., Rivard, M.-E., Beauchamp, C., Mercier, V., et al. (2022). Epigenetic reader SP140 loss of function drives Crohn's disease due to uncontrolled macrophage topoisomerases. Cell *185*, 3232-3247.e18. 10.1016/j.cell.2022.06.048.

39. Fraschilla, I., Amatullah, H., Rahman, R.-U., and Jeffrey, K.L. (2022). Immune chromatin reader SP140 regulates microbiota and risk for inflammatory bowel disease. Cell Host Microbe, S1931-3128(22)00417-6. 10.1016/j.chom.2022.08.018.

40. Mehta, S., Cronkite, D.A., Basavappa, M., Saunders, T.L., Adiliaghdam, F., Amatullah, H., Morrison, S.A., Pagan, J.D., Anthony, R.M., Tonnerre, P., et al. (2017). Maintenance of macrophage transcriptional programs and intestinal homeostasis by epigenetic reader SP140. Sci. Immunol. *2*, eaag3160. 10.1126/sciimmunol.aag3160.

41. Stoeckius, M., Hafemeister, C., Stephenson, W., Houck-Loomis, B., Chattopadhyay, P.K., Swerdlow, H., Satija, R., and Smibert, P. (2017). Simultaneous epitope and transcriptome measurement in single cells. Nat. Methods *14*, 865–868. 10.1038/nmeth.4380.

42. Hao, Y., Hao, S., Andersen-Nissen, E., Mauck, W.M., Zheng, S., Butler, A., Lee, M.J., Wilk, A.J., Darby, C., Zager, M., et al. (2021). Integrated analysis of multimodal single-cell data. Cell *184*, 3573-3587.e29. 10.1016/j.cell.2021.04.048.

43. Becht, E., McInnes, L., Healy, J., Dutertre, C.-A., Kwok, I.W.H., Ng, L.G., Ginhoux, F., and Newell, E.W. (2019). Dimensionality reduction for visualizing single-cell data using UMAP. Nat. Biotechnol. *37*, 38–44. 10.1038/nbt.4314.

44. Pisu, D., Huang, L., Narang, V., Theriault, M., Lê-Bury, G., Lee, B., Lakudzala, A.E., Mzinza, D.T., Mhango, D.V., Mitini-Nkhoma, S.C., et al. (2021). Single cell analysis of M. tuberculosis phenotype and macrophage lineages in the infected lung. J. Exp. Med. *218*, e20210615. 10.1084/jem.20210615.

45. Hu, J., Sealfon, S.C., Hayot, F., Jayaprakash, C., Kumar, M., Pendleton, A.C., Ganee, A., Fernandez-Sesma, A., Moran, T.M., and Wetmur, J.G. (2007). Chromosome-specific and noisy IFNB1 transcription in individual virus-infected human primary dendritic cells. Nucleic Acids Res. *35*, 5232–5241. 10.1093/nar/gkm557.

46. Scheu, S., Dresing, P., and Locksley, R.M. (2008). Visualization of IFNbeta production by plasmacytoid versus conventional dendritic cells under specific stimulation conditions in vivo. Proc. Natl. Acad. Sci. U. S. A. *105*, 20416–20421. 10.1073/pnas.0808537105.

47. Thomsen, E.A., Andersen, S., Marqvorsen, M.H.S., Skipper, K.A., Paludan, S.R., and Mikkelsen, J.G. (2021). Single-Cell Monitoring of Activated Innate Immune Signaling by a d2eGFP-Based Reporter Mimicking Time-Restricted Activation of IFNB1 Expression. Front. Cell. Infect. Microbiol. *11*, 784762. 10.3389/fcimb.2021.784762.

48. Zhao, M., Zhang, J., Phatnani, H., Scheu, S., and Maniatis, T. (2012). Stochastic expression of the interferon-β gene. PLoS Biol. *10*, e1001249. 10.1371/journal.pbio.1001249.

49. Esaulova, E., Das, S., Singh, D.K., Choreño-Parra, J.A., Swain, A., Arthur, L., Rangel-Moreno, J., Ahmed, M., Singh, B., Gupta, A., et al. (2021). The immune landscape in tuberculosis reveals populations linked to disease and latency. Cell Host Microbe *29*, 165-178.e8. 10.1016/j.chom.2020.11.013.

50. Madisen, L., Zwingman, T.A., Sunkin, S.M., Oh, S.W., Zariwala, H.A., Gu, H., Ng, L.L., Palmiter, R.D., Hawrylycz, M.J., Jones, A.R., et al. (2010). A robust and high-throughput Cre reporting and characterization system for the whole mouse brain. Nat. Neurosci. *13*, 133–140. 10.1038/nn.2467.

51. Fitzgerald-Bocarsly, P., Dai, J., and Singh, S. (2008). Plasmacytoid dendritic cells and type I IFN: 50 years of convergent history. Cytokine Growth Factor Rev. *19*, 3–19. 10.1016/j.cytogfr.2007.10.006.

52. Gerner, M.Y., Kastenmuller, W., Ifrim, I., Kabat, J., and Germain, R.N. (2012). Histo-cytometry: a method for highly multiplex quantitative tissue imaging analysis applied to dendritic cell subset microanatomy in lymph nodes. Immunity *37*, 364–376. 10.1016/j.immuni.2012.07.011.

53. Kotov, D.I., Pengo, T., Mitchell, J.S., Gastinger, M.J., and Jenkins, M.K. (2019). Chrysalis: A New Method for High-Throughput Histo-Cytometry Analysis of Images and Movies. J. Immunol. *202*, 300–308. 10.4049/jimmunol.1801202.

54. Cervantes-Barragan, L., Lewis, K.L., Firner, S., Thiel, V., Hugues, S., Reith, W., Ludewig, B., and Reizis, B. (2012). Plasmacytoid dendritic cells control T-cell response to chronic viral infection. Proc. Natl. Acad. Sci. *109*, 3012–3017. 10.1073/pnas.1117359109.

55. Smit, J.J., Rudd, B.D., and Lukacs, N.W. (2006). Plasmacytoid dendritic cells inhibit pulmonary immunopathology and promote clearance of respiratory syncytial virus. J. Exp. Med. *203*, 1153–1159. 10.1084/jem.20052359.

56. Asselin-Paturel, C., Brizard, G., Pin, J.-J., Brière, F., and Trinchieri, G. (2003). Mouse strain differences in plasmacytoid dendritic cell frequency and function revealed by a novel monoclonal antibody. J. Immunol. Baltim. Md 1950 *171*, 6466–6477. 10.4049/jimmunol.171.12.6466.

57. Blasius, A.L., Giurisato, E., Cella, M., Schreiber, R.D., Shaw, A.S., and Colonna, M. (2006). Bone marrow stromal cell antigen 2 is a specific marker of type I IFN-producing cells in the naive mouse, but a promiscuous cell surface antigen following IFN stimulation. J. Immunol. Baltim. Md 1950 *177*, 3260–3265. 10.4049/jimmunol.177.5.3260.

58. Krug, A., French, A.R., Barchet, W., Fischer, J.A.A., Dzionek, A., Pingel, J.T., Orihuela, M.M., Akira, S., Yokoyama, W.M., and Colonna, M. (2004). TLR9-dependent recognition of MCMV by IPC and DC generates coordinated cytokine responses that activate antiviral NK cell function. Immunity *21*, 107–119. 10.1016/j.immuni.2004.06.007.

59. Swiecki, M., Gilfillan, S., Vermi, W., Wang, Y., and Colonna, M. (2010). Plasmacytoid dendritic cell ablation impacts early interferon responses and antiviral NK and CD8(+) T cell accrual. Immunity *33*, 955–966. 10.1016/j.immuni.2010.11.020.

60. Cervantes-Luevano, K.E., Caronni, N., Castiello, M.C., Fontana, E., Piperno, G.M., Naseem, A., Uva, P., Bosticardo, M., Marcovecchio, G.E., Notarangelo, L.D., et al. (2018). Neutrophils drive type I interferon production and autoantibodies in patients with Wiskott-Aldrich syndrome. J. Allergy Clin. Immunol. *142*, 1605-1617.e4. 10.1016/j.jaci.2017.11.063.

61. Moreira-Teixeira, L., Stimpson, P.J., Stavropoulos, E., Hadebe, S., Chakravarty, P., Ioannou, M., Aramburu, I.V., Herbert, E., Priestnall, S.L., Suarez-Bonnet, A., et al. (2020). Type I IFN exacerbates disease in tuberculosis-susceptible mice by inducing neutrophil-mediated lung inflammation and NETosis. Nat. Commun. *11*, 5566. 10.1038/s41467-020-19412-6.

62. de Weerd, N.A., and Nguyen, T. (2012). The interferons and their receptors—distribution and regulation. Immunol. Cell Biol. *90*, 483–491. 10.1038/icb.2012.9.

63. Nilsson, A., Peters, J.M., Meimetis, N., Bryson, B., and Lauffenburger, D.A. (2022). Artificial neural networks enable genome-scale simulations of intracellular signaling. Nat. Commun. *13*, 3069. 10.1038/s41467-022-30684-y.

64. Crisler, W.J., and Lenz, L.L. (2018). Crosstalk between type I and II interferons in regulation of myeloid cell responses during bacterial infection. Curr. Opin. Immunol. *54*, 35–41. 10.1016/j.coi.2018.05.014.

65. Scriba, T.J., Penn-Nicholson, A., Shankar, S., Hraha, T., Thompson, E.G., Sterling, D., Nemes, E., Darboe, F., Suliman, S., Amon, L.M., et al. (2017). Sequential inflammatory processes define human progression from M. tuberculosis infection to tuberculosis disease. PLOS Pathog. *13*, e1006687. 10.1371/journal.ppat.1006687.

66. Bohrer, A.C., Tocheny, C., Assmann, M., Ganusov, V.V., and Mayer-Barber, K.D. (2018). Cutting Edge: IL-1R1 Mediates Host Resistance to Mycobacterium tuberculosis by Trans-Protection of Infected Cells. J. Immunol. Baltim. Md 1950 *201*, 1645–1650. 10.4049/jimmunol.1800438.

67. Mayer-Barber, K.D., Andrade, B.B., Barber, D.L., Hieny, S., Feng, C.G., Caspar, P., Oland, S., Gordon, S., and Sher, A. (2011). Innate and Adaptive Interferons Suppress IL-1α and IL-1β Production by Distinct Pulmonary Myeloid Subsets during Mycobacterium tuberculosis Infection. Immunity *35*, 1023–1034. 10.1016/j.immuni.2011.12.002.

68. Boehme, K.W., Singh, J., Perry, S.T., and Compton, T. (2004). Human cytomegalovirus elicits a coordinated cellular antiviral response via envelope glycoprotein B. J. Virol. *78*, 1202–1211. 10.1128/jvi.78.3.1202-1211.2004.

69. DeFilippis, V.R., Alvarado, D., Sali, T., Rothenburg, S., and Früh, K. (2010). Human Cytomegalovirus Induces the Interferon Response via the DNA Sensor ZBP1. J. Virol. *84*, 585–598. 10.1128/JVI.01748-09.

70. Paijo, J., Döring, M., Spanier, J., Grabski, E., Nooruzzaman, M., Schmidt, T., Witte, G., Messerle, M., Hornung, V., Kaever, V., et al. (2016). cGAS Senses Human Cytomegalovirus and Induces Type I Interferon Responses in Human Monocyte-Derived Cells. PLoS Pathog. *12*, e1005546. 10.1371/journal.ppat.1005546.

71. Lowe, D.M., Bandara, A.K., Packe, G.E., Barker, R.D., Wilkinson, R.J., Griffiths, C.J., and Martineau, A.R. (2013). Neutrophilia independently predicts death in tuberculosis. Eur. Respir. J. *42*, 1752–1757. 10.1183/09031936.00140913.

72. Panteleev, A.V., Nikitina, I.Y., Burmistrova, I.A., Kosmiadi, G.A., Radaeva, T.V., Amansahedov, R.B., Sadikov, P.V., Serdyuk, Y.V., Larionova, E.E., Bagdasarian, T.R., et al. (2017). Severe Tuberculosis in Humans Correlates Best with Neutrophil Abundance and Lymphocyte Deficiency and Does Not Correlate with Antigen-Specific CD4 T-Cell Response. Front. Immunol. *8*.

73. Akter, S., Chauhan, K.S., Dunlap, M.D., Choreño-Parra, J.A., Lu, L., Esaulova, E., Zúñiga, J., Artyomov, M.N., Kaushal, D., and Khader, S.A. (2022). Mycobacterium tuberculosis infection drives a type I IFN signature in lung lymphocytes. Cell Rep. *39*, 110983. 10.1016/j.celrep.2022.110983.

74. Manca, C., Tsenova, L., Bergtold, A., Freeman, S., Tovey, M., Musser, J.M., Barry, C.E., Freedman, V.H., and Kaplan, G. (2001). Virulence of a Mycobacterium tuberculosis clinical isolate in mice is determined by failure to induce Th1 type immunity and is associated with induction of IFN-alpha /beta. Proc. Natl. Acad. Sci. U. S. A. *98*, 5752–5757. 10.1073/pnas.091096998.

75. Howard, N.C., Marin, N.D., Ahmed, M., Rosa, B.A., Martin, J., Bambouskova, M., Sergushichev, A., Loginicheva, E., Kurepina, N., Rangel-Moreno, J., et al. (2018). Mycobacterium tuberculosis carrying a rifampicin drug resistance mutation reprograms macrophage metabolism through cell wall lipid changes. Nat. Microbiol. *3*, 1099–1108. 10.1038/s41564-018-0245-0.

76. Ordway, D., Henao-Tamayo, M., Harton, M., Palanisamy, G., Troudt, J., Shanley, C., Basaraba, R.J., and Orme, I.M. (2007). The Hypervirulent Mycobacterium tuberculosis Strain HN878 Induces a Potent TH1 Response followed by Rapid Down-Regulation. J. Immunol. *179*, 522–531. 10.4049/jimmunol.179.1.522.

77. Crother, T.R., Ma, J., Jupelli, M., Chiba, N., Chen, S., Slepenkin, A., Alsabeh, R., Peterson, E., Shimada, K., and Arditi, M. (2012). Plasmacytoid Dendritic Cells Play a Role for Effective Innate Immune Responses during Chlamydia pneumoniae Infection in Mice. PLOS ONE *7*, e48655. 10.1371/journal.pone.0048655.

78. Lippitsch, A., Baal, N., Chukovetskyi, Y., Cunningham, S., Michel, G., Dietert, K., Gurtner, C., Gruber, A.D., Bein, G., and Hackstein, H. (2019). Plasmacytoid dendritic cell depletion

modifies FoxP3+ T cell homeostasis and the clinical course of bacterial pneumonia in mice. J. Leukoc. Biol. *106*, 977–985. 10.1002/JLB.3AB0119-014RR.

79. Rahman, T., Brown, A.S., Hartland, E.L., van Driel, I.R., and Fung, K.Y. (2019). Plasmacytoid Dendritic Cells Provide Protection Against Bacterial-Induced Colitis. Front. Immunol. *10*.

80. Wu, V., Smith, A.A., You, H., Nguyen, T.A., Ferguson, R., Taylor, M., Park, J.E., Llontop, P., Youngman, K.R., and Abramson, T. (2016). Plasmacytoid dendritic cell-derived IFNα modulates Th17 differentiation during early Bordetella pertussis infection in mice. Mucosal Immunol. *9*, 777–786. 10.1038/mi.2015.101.

81. Lichtner, M., Rossi, R., Mengoni, F., Vignoli, S., Colacchia, B., Massetti, A.P., Kamga, I., Hosmalin, A., Vullo, V., and Mastroianni, C.M. (2006). Circulating dendritic cells and interferon-α production in patients with tuberculosis: correlation with clinical outcome and treatment response. Clin. Exp. Immunol. *143*, 329–337. 10.1111/j.1365-2249.2005.02994.x.

82. Lu, Y.-B., Xiao, D.-Q., Liang, K.-D., Zhang, J.-A., Wang, W.-D., Yu, S.-Y., Zheng, B.-Y., Gao, Y.-C., Dai, Y.-C., Jia, Y., et al. (2017). Profiling dendritic cell subsets in the patients with active pulmonary tuberculosis. Mol. Immunol. *91*, 86–96. 10.1016/j.molimm.2017.08.007.

83. Gideon, H.P., Hughes, T.K., Tzouanas, C.N., Wadsworth, M.H., Tu, A.A., Gierahn, T.M., Peters, J.M., Hopkins, F.F., Wei, J.-R., Kummerlowe, C., et al. (2022). Multimodal profiling of lung granulomas in macaques reveals cellular correlates of tuberculosis control. Immunity *55*, 827-846.e10. 10.1016/j.immuni.2022.04.004.

84. Caielli, S., Athale, S., Domic, B., Murat, E., Chandra, M., Banchereau, R., Baisch, J., Phelps, K., Clayton, S., Gong, M., et al. (2016). Oxidized mitochondrial nucleoids released by neutrophils drive type I interferon production in human lupus. J. Exp. Med. *213*, 697–713. 10.1084/jem.20151876.

85. Bryson, B.D., Rosebrock, T.R., Tafesse, F.G., Itoh, C.Y., Nibasumba, A., Babunovic, G.H., Corleis, B., Martin, C., Keegan, C., Andrade, P., et al. (2019). Heterogeneous GM-CSF signaling in macrophages is associated with control of Mycobacterium tuberculosis. Nat. Commun. *10*, 2329. 10.1038/s41467-019-10065-8.

86. Gschwend, J., Sherman, S.P.M., Ridder, F., Feng, X., Liang, H.-E., Locksley, R.M., Becher, B., and Schneider, C. (2021). Alveolar macrophages rely on GM-CSF from alveolar epithelial type 2 cells before and after birth. J. Exp. Med. *218*, e20210745. 10.1084/jem.20210745.

87. Liu, X., Boyer, M.A., Holmgren, A.M., and Shin, S. (2020). Legionella-Infected Macrophages Engage the Alveolar Epithelium to Metabolically Reprogram Myeloid Cells and Promote Antibacterial Inflammation. Cell Host Microbe *28*, 683-698.e6. 10.1016/j.chom.2020.07.019.

88. Rothchild, A.C., Jayaraman, P., Nunes-Alves, C., and Behar, S.M. (2014). iNKT Cell Production of GM-CSF Controls Mycobacterium tuberculosis. PLOS Pathog. *10*, e1003805. 10.1371/journal.ppat.1003805.

89. Müller, U., Steinhoff, U., Reis, L.F., Hemmi, S., Pavlovic, J., Zinkernagel, R.M., and Aguet, M. (1994). Functional role of type I and type II interferons in antiviral defense. Science *264*, 1918–1921. 10.1126/science.8009221.

90. Prigge, J.R., Hoyt, T.R., Dobrinen, E., Capecchi, M.R., Schmidt, E.E., and Meissner, N. (2015). Type I IFNs Act upon Hematopoietic Progenitors To Protect and Maintain Hematopoiesis during Pneumocystis Lung Infection in Mice. J. Immunol. *195*, 5347–5357. 10.4049/jimmunol.1501553.

91. Passegué, E., Wagner, E.F., and Weissman, I.L. (2004). JunB deficiency leads to a myeloproliferative disorder arising from hematopoietic stem cells. Cell *119*, 431–443. 10.1016/j.cell.2004.10.010.

92. Clausen, B.E., Burkhardt, C., Reith, W., Renkawitz, R., and Förster, I. (1999). Conditional gene targeting in macrophages and granulocytes using LysMcre mice. Transgenic Res. *8*, 265–277. 10.1023/a:1008942828960.

93. Scott, C.L., T'Jonck, W., Martens, L., Todorov, H., Sichien, D., Soen, B., Bonnardel, J., Prijck, S.D., Vandamme, N., Cannoodt, R., et al. (2018). The Transcription Factor ZEB2 Is Required to Maintain the Tissue-Specific Identities of Macrophages. Immunity *49*, 312-325.e5. 10.1016/j.immuni.2018.07.004.

94. Jaye, D.L., Geigerman, C.M., Herling, M., Eastburn, K., Waller, E.K., and Jones, D. (2006). Expression of the plasmacytoid dendritic cell marker BDCA-2 supports a spectrum of maturation among CD4+ CD56+ hematodermic neoplasms. Mod. Pathol. Off. J. U. S. Can. Acad. Pathol. Inc *19*, 1555–1562. 10.1038/modpathol.3800679.

95. Jaye, D.L., Iqbal, J., Fujita, N., Geigerman, C.M., Li, S., Karanam, S., Fu, K., Weisenburger, D.D., Chan, W.C., Moreno, C.S., et al. (2007). The BCL6-associated transcriptional co-repressor, MTA3, is selectively expressed by germinal centre B cells and lymphomas of putative germinal centre derivation. J. Pathol. *213*, 106–115. 10.1002/path.2199.

96. Stoeckius, M., Zheng, S., Houck-Loomis, B., Hao, S., Yeung, B.Z., Mauck, W.M., Smibert, P., and Satija, R. (2018). Cell Hashing with barcoded antibodies enables multiplexing and doublet detection for single cell genomics. Genome Biol. *19*, 224. 10.1186/s13059-018-1603-1.

97. Roelli, P., bbimber, Flynn, B., santiagorevale, and Gui, G. (2019). Hoohm/CITE-seq-Count: 1.4.2. 10.5281/zenodo.2590196.

98. Andreatta, M., and Carmona, S.J. (2021). UCell: robust and scalable single-cell gene signature scoring. 2021.04.13.439670. 10.1101/2021.04.13.439670.

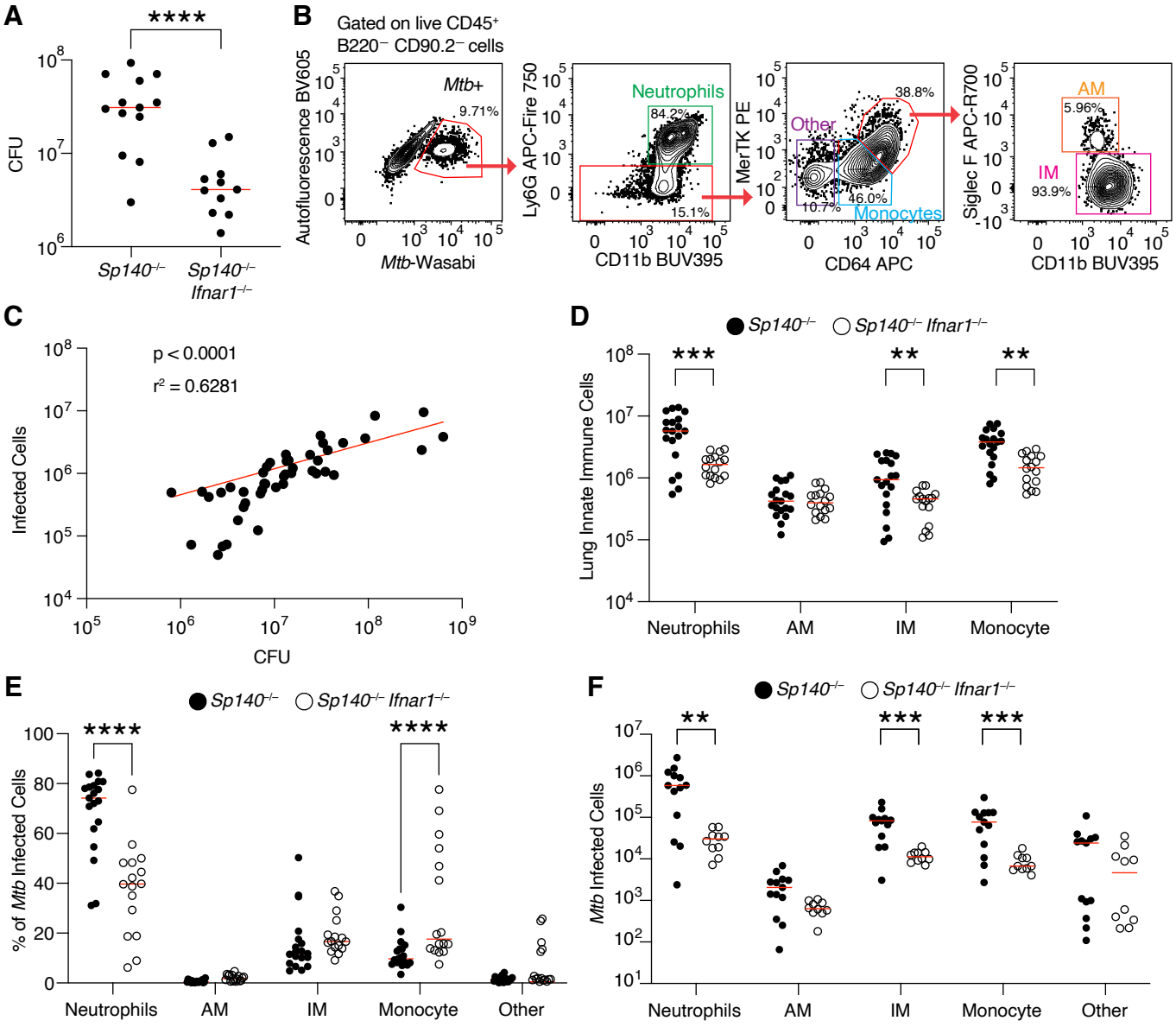

Figure 1. Myeloid cells are the dominant *Mtb* harboring cells in *Sp140*$^{-/-}$ and *Sp140*$^{-/-}$ *Ifnar1*$^{-/-}$ mice. (**A**) Colony forming units of *Mtb* in the lungs of *Sp140*$^{-/-}$ (n = 13) and *Sp140*$^{-/-}$ *Ifnar1*$^{-/-}$ (n = 11) mice 25 days post-infection. (**B**) Representative flow cytometry plots of an *Mtb*-infected *Sp140*$^{-/-}$ mouse lung gated on live CD45^{+} B220^{-} CD90.2^{-} cells to identify *Mtb*-infected cells, subset into neutrophils (green; Ly6G^{+} CD11b^{+}), other cells (purple; Ly6G^{-} CD64^{-} MerTK^{-}), monocytes (blue; Ly6G^{-} CD64^{+} MerTK^{low}), alveolar macrophages (AMs; orange; Ly6G^{-} CD64^{+} MerTK^{high} Siglec F^{+}), and interstitial macrophages (IMs; pink; Ly6G^{-} CD64^{+} MerTK^{high} Siglec F^{-}). (**C**) Correlation between the number of infected cells identified by flow cytometry of total lung digests gated as in Fig. 1B to the colony forming units from the same infected lung (*Sp140*$^{-/-}$ and *Sp140*$^{-/-}$ *Ifnar1*$^{-/-}$ combined; n = 45). The red line indicates a nonlinear regression of the displayed data. (**D**) Number of innate immune cells by cell type in the lungs of *Mtb*-infected *Sp140*$^{-/-}$ (n = 19; closed circles) and *Sp140*$^{-/-}$ *Ifnar1*$^{-/-}$ mice (n = 16; open circles). (**E**) Frequency and (**F**) number by immune cell population of *Mtb*-infected cells in *Sp140*$^{-/-}$ (n = 12-19; closed circles) and *Sp140*$^{-/-}$ *Ifnar1*$^{-/-}$ mice (n = 10-15; open circles). Lungs were analyzed for the depicted experiments 24-26 days after *Mtb* infection. The bars in (A), (D), (E), and (F) represent the median. Pooled data from two or three independent experiments are shown. A linear regression performed on log transformed data was used to calculate significance and R^2 for (C). An unpaired t test was used to determine significance for (A), a two-way ANOVA with Sidak's multiple comparisons test was used to calculate significance for (D), (E), and (F). **$p < 0.01$, ***$p < 0.001$, ****$p < 0.0001$.

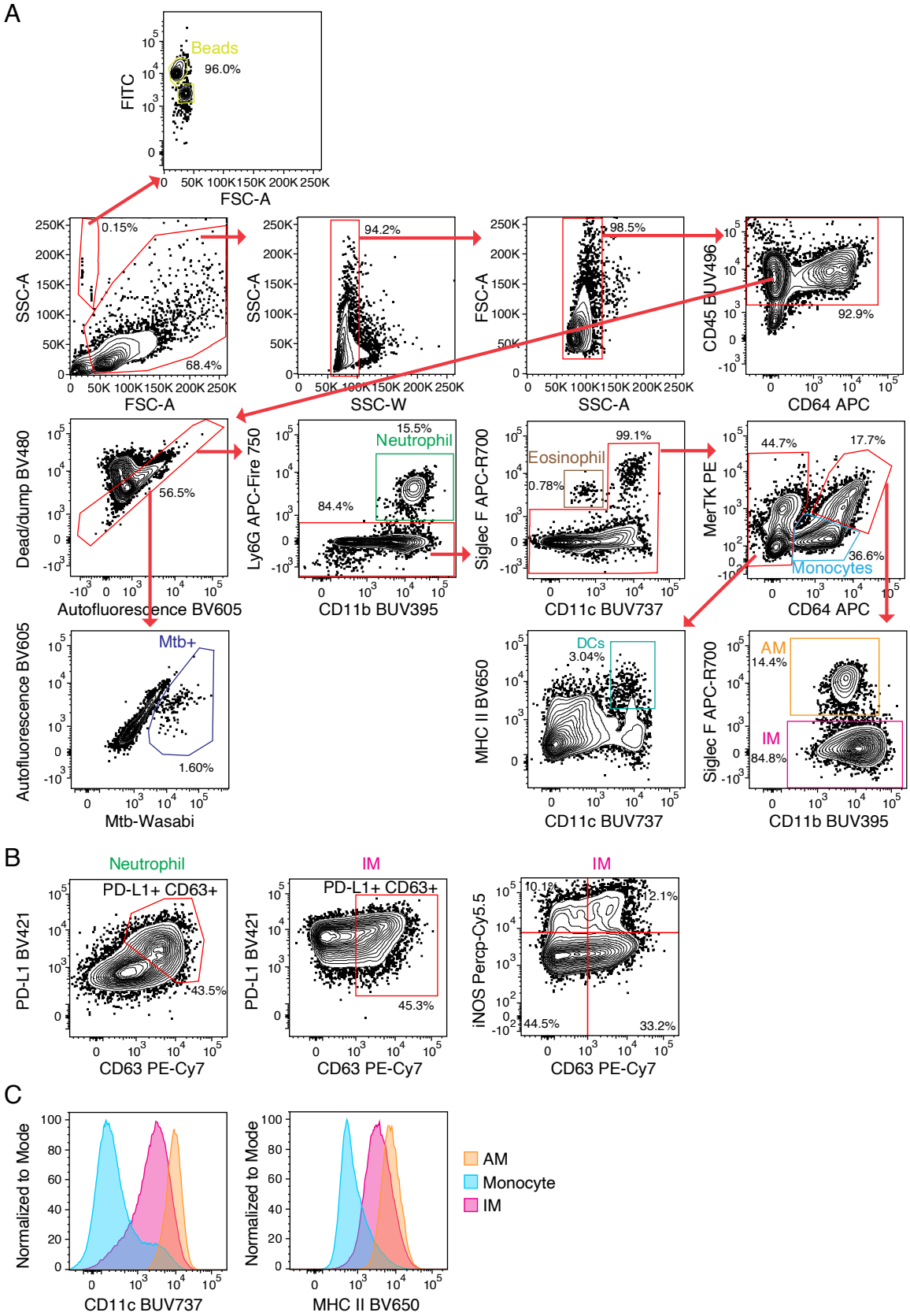

Supplementary Figure 1. Representative flow cytometry gating strategy to identify innate immune cell populations in *Mtb*-infected lungs. (**A**) Gating strategy for identifying neutrophils, eosinophils, monocytes, dendritic cells (DCs), alveolar macrophages (AMs), interstitial macrophages (IMs), and Mtb infected cells. Very few *Mtb*⁺ cells were detected among the lymphoid and non-hematopoietic-derived cells (**B**) Representative identification of activated (CD63⁺ PD-L1⁺ or iNOS⁺) neutrophils and interstitial macrophages in tuberculosis infected lungs. (**C**) Histogram comparing CD11c and MHC II expression on AMs (orange), monocytes (blue), and IMs (red).

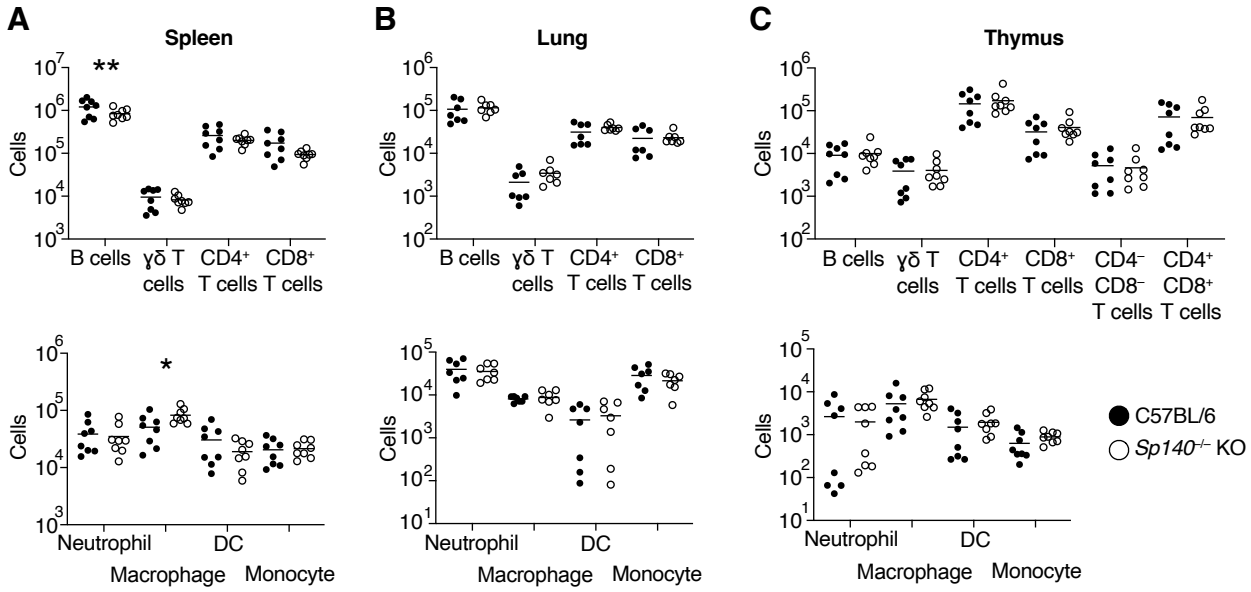

Supplementary Figure 2. Naïve *Sp140*$^{-/-}$ mice exhibit minimally altered immune cell numbers by flow cytometry. Comparison of innate and adaptive immune cell numbers between B6 (n = 7; closed circles) and *Sp140*$^{-/-}$ (n = 8; open circles) (**A**) spleen, (**B**) lung, (**C**) and thymus. The bars in (A), (B), and (C) represent the median. Pooled data from two independent experiments are shown in (A), (B), and (C). Statistical significance was calculated by multiple unpaired t tests in (A), (B), and (C).

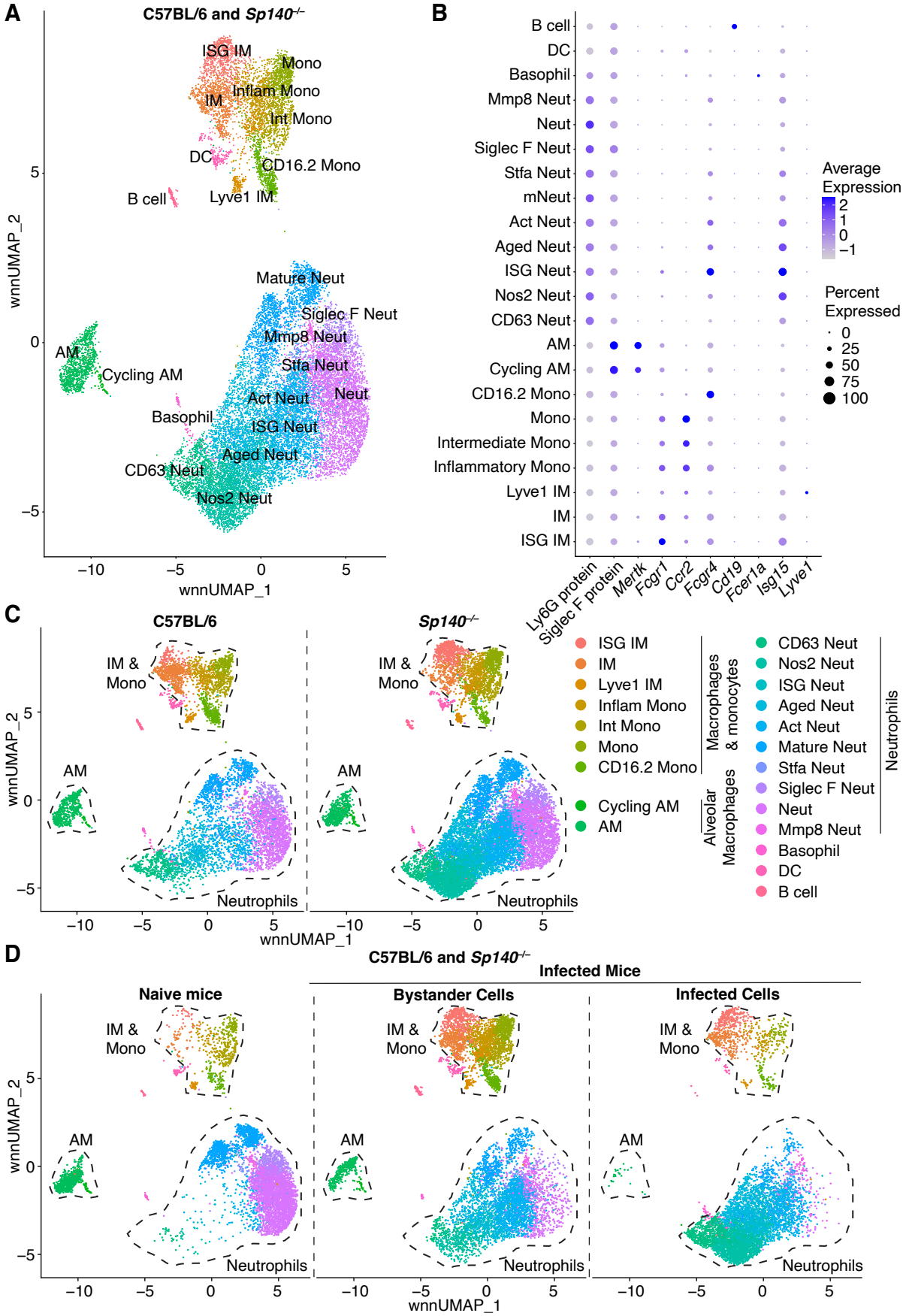

Figure 2. ScRNA-sequencing analysis of B6 and *Sp140*$^{-/-}$ myeloid cells from *Mtb* infected and naïve lungs. CITE-seq was used to perform scRNA-sequencing analysis to integrate transcriptomic and protein expression of single cells, as described further in Supplementary Fig. 3. (**A**) Weighted nearest neighbor UMAP plot depicting unbiased clustering of myeloid cells combining all cells from wild-type B6 and *Sp140*$^{-/-}$ *Mtb*-infected and naïve lungs (n = 10 lungs; n= 20272 cells). (**B**) Dot plot of lineage defining protein and mRNA markers used to annotate the dataset. (**C**) Weighted nearest neighbor UMAP plot comparing cells from B6 and *Sp140*$^{-/-}$ lungs. (**D**) Weighted nearest neighbor UMAP plot contrasting cells from naïve mice, the bystander cells from *Mtb*-infected mice, and the *Mtb*-infected cells from *Mtb*-infected mice (B6 and *Sp140*$^{-/-}$ combined). Lungs were analyzed for the depicted experiment 25 days after *Mtb*-Wasabi infection. For each genotype, n = 3 for the infected lung samples and n = 2 for the naïve lung samples. *$p < 0.05$, **$p < 0.01$.

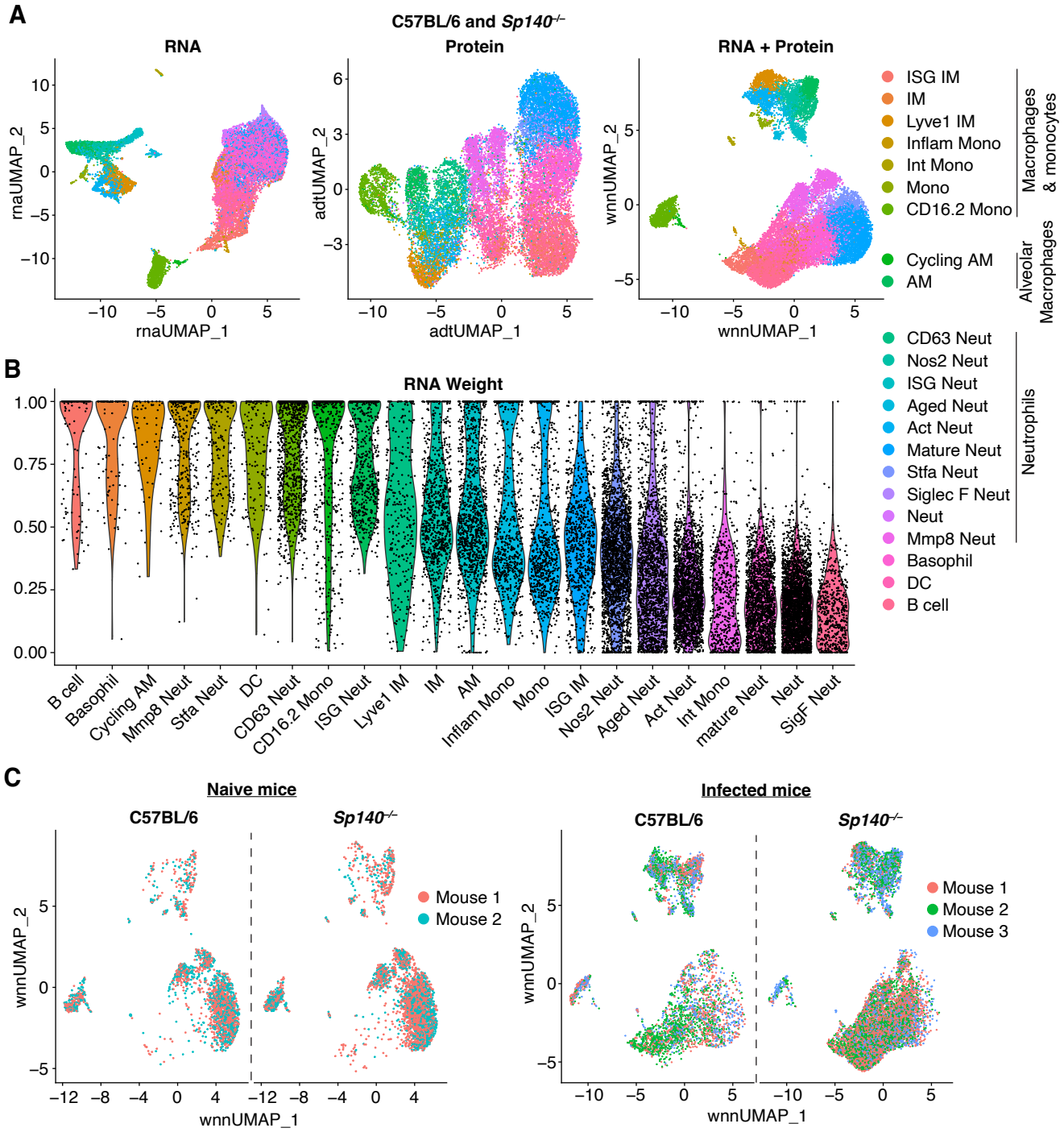

Supplementary Figure 3. The scRNA-seq dataset is a CITE-seq experiment that represents multiple mice and combines mRNA and protein expression. (**A**) UMAP plots depicting cell clustering by mRNA expression, protein expression, or combined mRNA and protein expression (B6 and *Sp140*$^{-/-}$ combined). (**B**) Violin plot of the RNA weight of each cluster, thereby depicting clusters identified based primarily on mRNA (closer to RNA weight = 1) or protein (closer to RNA weight = 0; B6 and *Sp140*$^{-/-}$ combined). (**C**) Weighted nearest neighbor UMAP plot of the biological replicates from naïve and infected B6 and *Sp140*$^{-/-}$ mice. For each genotype, n = 3 for the infected lung samples and n = 2 for the naïve lung samples.

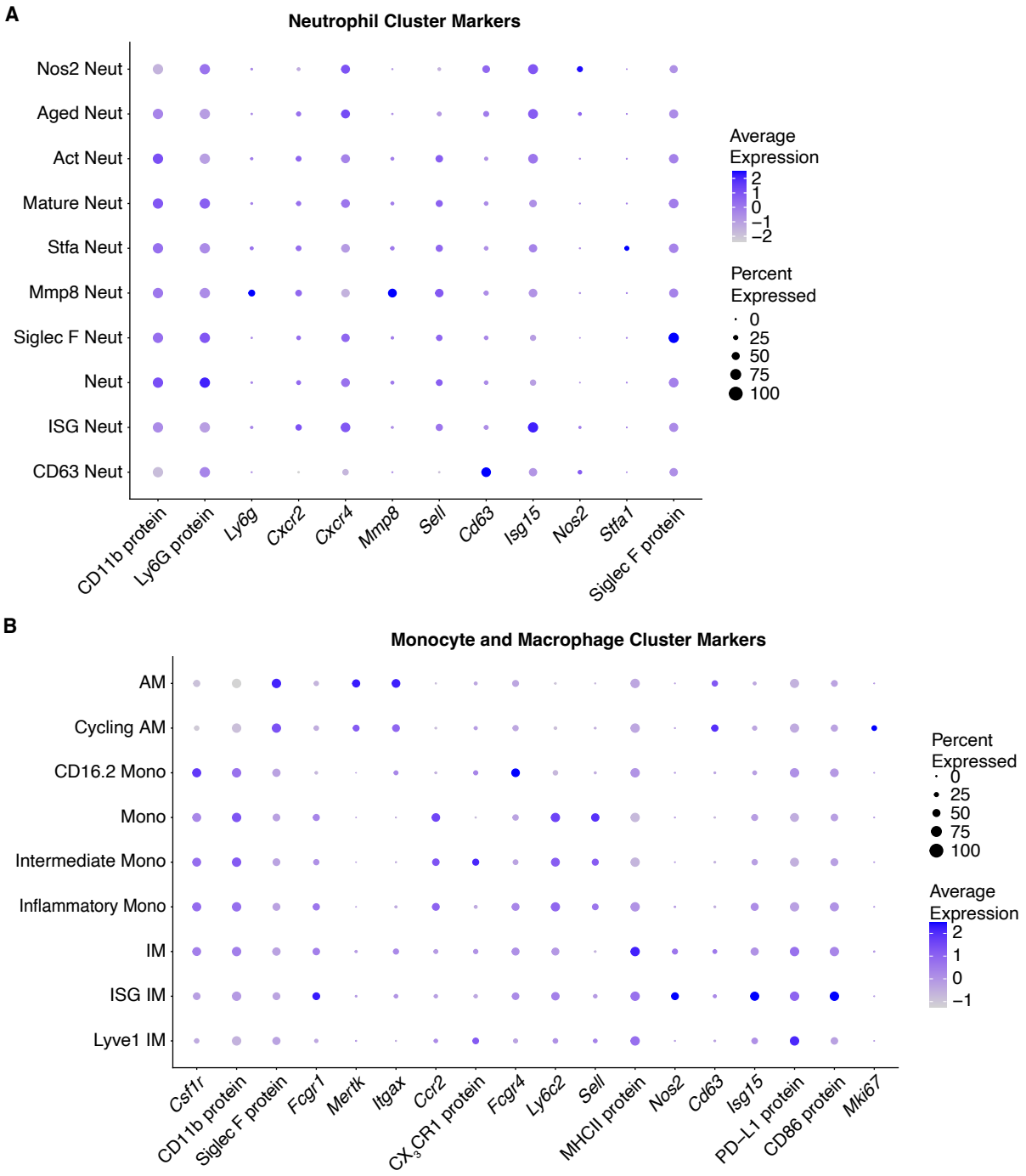

Supplementary Figure 4. The expression of protein and mRNA used to annotate the myeloid cell clusters in the scRNA-seq dataset. Markers used for annotating (**A**) neutrophil and (**B**) monocyte and macrophage clusters based on maturity, activation status, and unique gene expression. The data represents a total of 10 mice (n = 3 for the infected lung samples and n = 2 for the naïve lung samples from B6 and *Sp140*$^{-/-}$ mice).

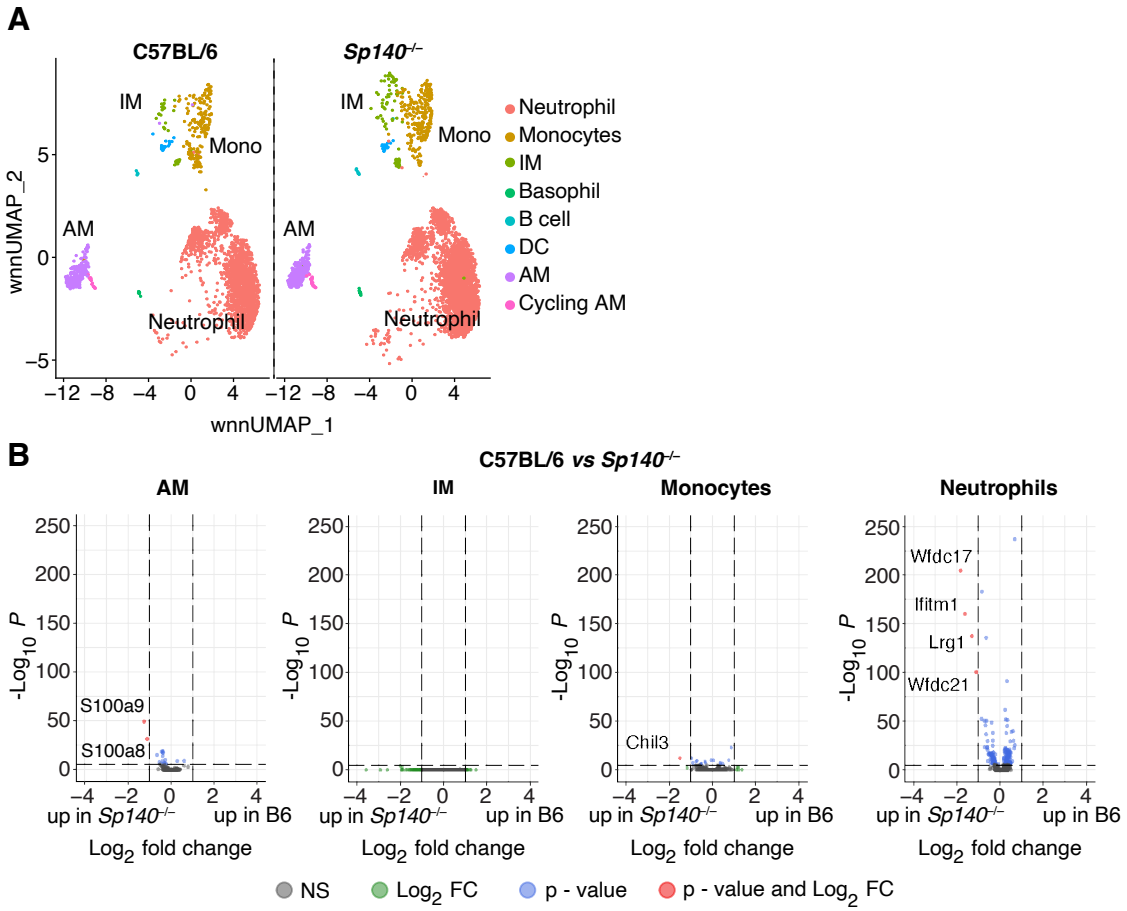

Supplementary Figure 5. Naïve *Sp140*$^{-/-}$ mice do not exhibit increased inflammation by scRNA-seq. (**A**) Weighted nearest neighbor UMAP plot of myeloid cells from naïve lungs of B6 (n = 2) and *Sp140*$^{-/-}$ (n = 2) mice. (**B**) Volcano plot of the differentially expressed genes between B6 and *Sp140*$^{-/-}$ alveolar macrophages (AMs), interstitial macrophages (IMs), monocytes, and neutrophils. Greater fold change indicates higher expression in B6 relative to *Sp140*$^{-/-}$. Statistical significance in (B) was calculated with the Wilcoxon Rank-Sum test.

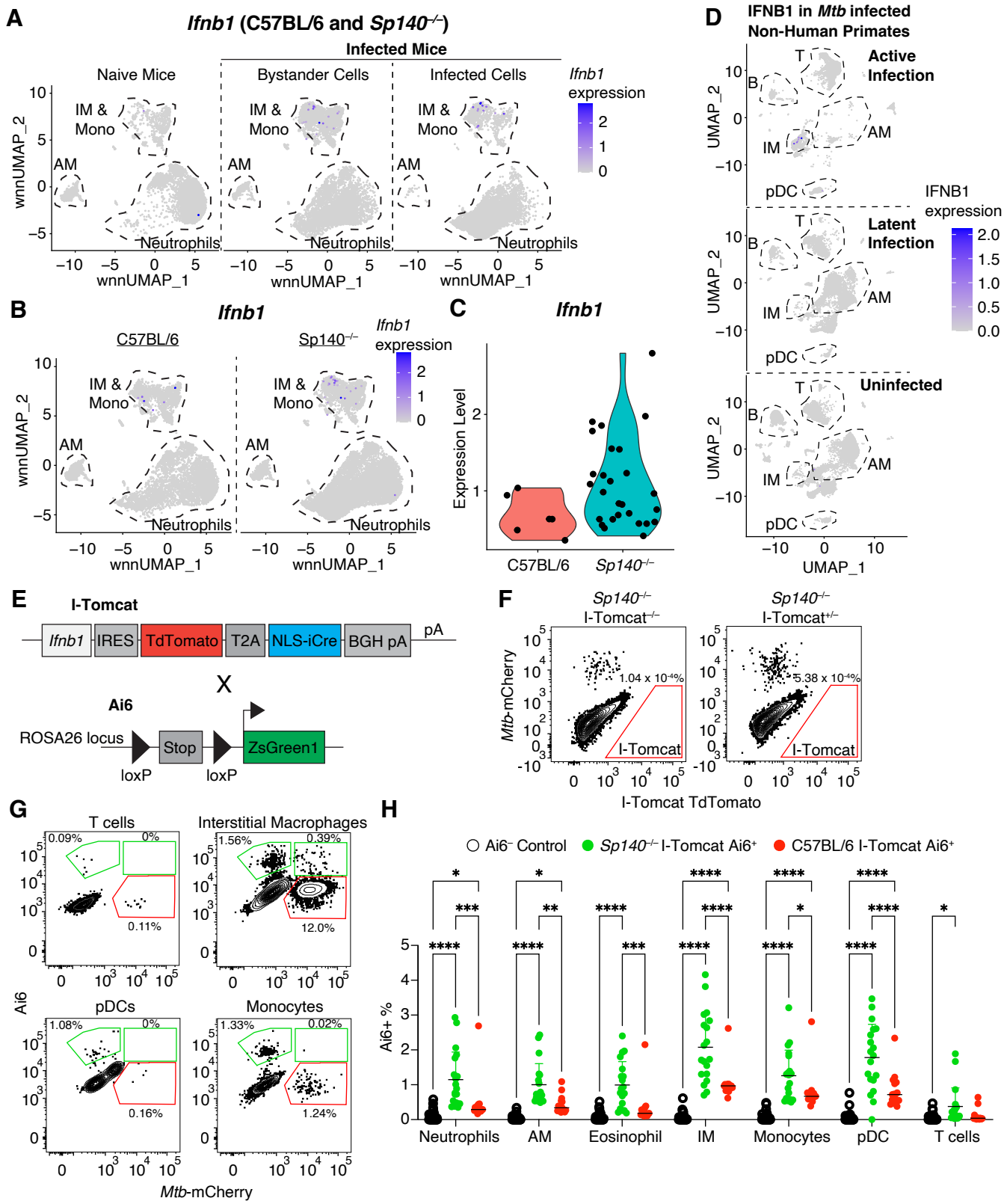

Figure 3. Interstitial macrophages, monocytes, and plasmacytoid dendritic cells are the primary IFN-β producers in mice and non-human primates. (**A**) Weighted nearest neighbor UMAP plot of *Ifnb1* expression in myeloid cells from naïve mice, bystander myeloid cells from infected mice, and *Mtb*-infected myeloid cells from infected mice (B6 and *Sp140*$^{-/-}$ combined). (**B**) Weighted nearest neighbor UMAP plot of *Ifnb1* expression in myeloid cells from B6 and *Sp140*$^{-/-}$ mice. (**C**) Violin plot depicting level of *Ifnb1* expression in B6 and *Sp140*$^{-/-}$ cells that express *Ifnb1*. (**D**) Analysis of GSE149758 scRNA-seq data from Esaulova E., et al. 2021. UMAP depicting IFNB1 expression in cells from non-human primates with active *Mtb* infection, latent *Mtb* infection, or that are uninfected. (**E**) Schematic representation of the genetic structure of I-Tomcat mice and Ai6 mice. Cre expression permanently deletes the loxP-flanked STOP cassette resulting in constitutive ZsGreen expression. (**F**) Representative flow cytometry plot indicating lack of detectable TdTomato expression in immune cells. (**G**) Representative flow cytometry plots of ZsGreen expression and *Mtb*-mCherry detection in T cells, IMs, pDCs, and monocytes. (**H**) Frequency of Ai6 expressing cells in lung immune cells from Ai6^{-} control (n = 34; open circles), *Sp140*$^{-/-}$ I-Tomcat Ai6 (n = 19; green circles), and I-Tomcat Ai6 (n = 15; red circles) mice. The bars in (H) represent the median. Pooled data from four independent experiments are shown in (H). Lungs were analyzed for the depicted experiments 25 days after *Mtb* infection. Statistical significance in (H) was calculated by one-way ANOVA with Tukey's multiple comparison test. *p < 0.05, **p < 0.01, ***p < 0.001, ****p < 0.0001.

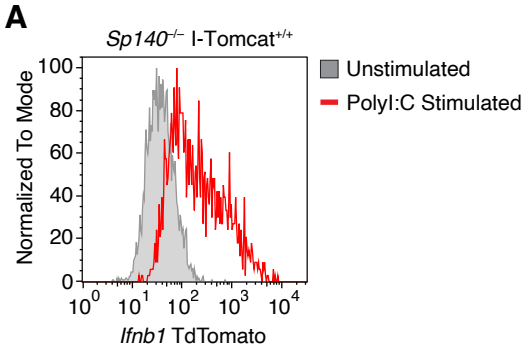

Supplementary Figure 6. I-Tomcat bone marrow-derived macrophages express TdTomato following poly I:C stimulation. (**A**) Representative flow cytometry plot of TdTomato expression by I-Tomcat bone marrow-derived macrophages that were unstimulated (grey) or stimulated with poly I:C (red line).

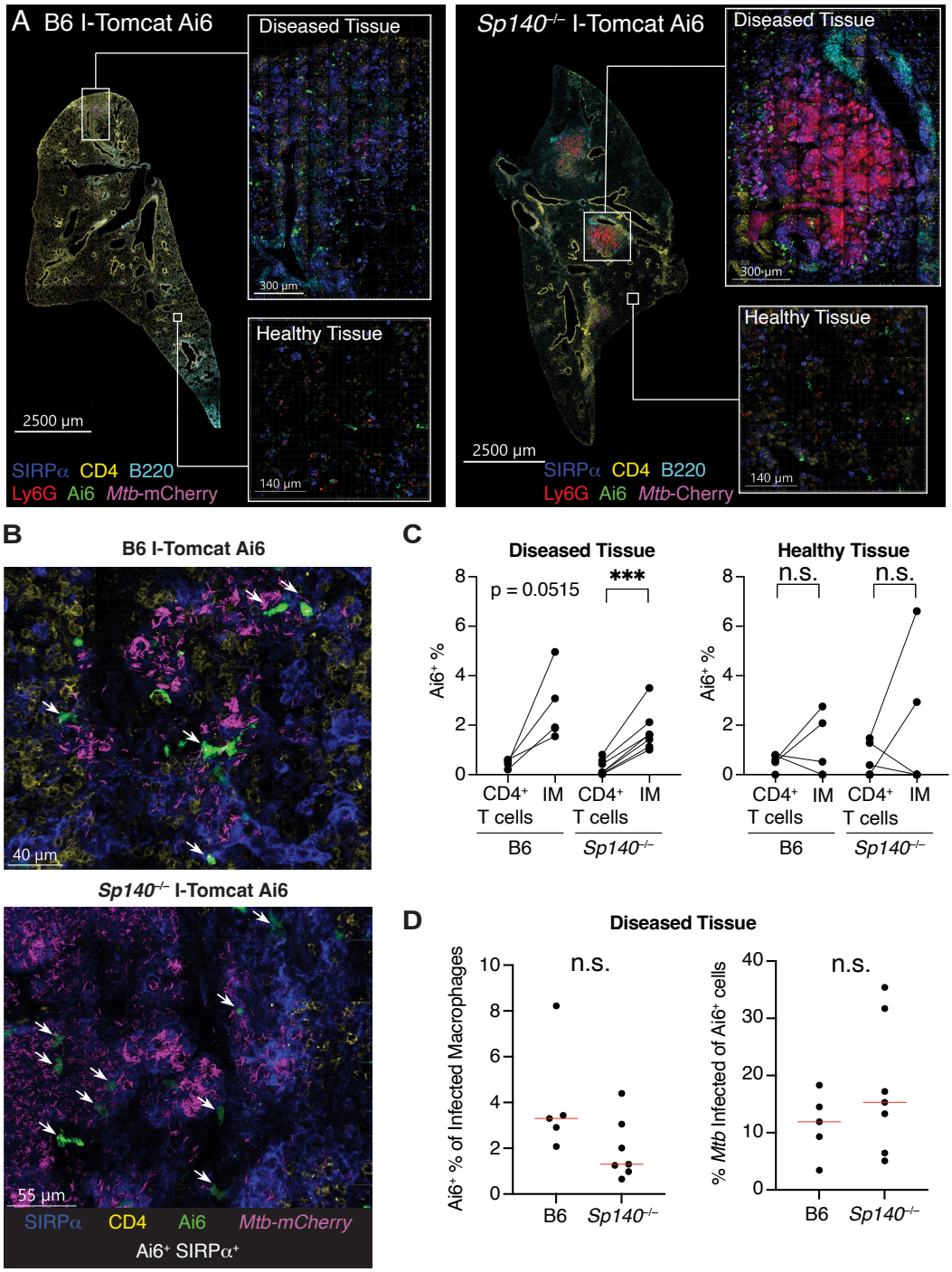

Figure 4. Cells producing IFN-β are enriched in diseased tissue, but only a minority harbor *Mtb*. (**A**) Representative images of *Mtb*-infected I-Tomcat Ai6 and *Sp140*$^{-/-}$ I-Tomcat Ai6 lung sections stained for SIRPα (dark blue), CD4 (yellow), B220 (teal), Ly6G (red), Ai6 (green), and *Mtb*-expressed mCherry (magenta). Inset images depict higher magnification of diseased and healthy tissue for both genotypes. (**B**) Representative images of Ai6^{+} cell localization near *Mtb* in the diseased portions of I-Tomcat Ai6 and *Sp140*$^{-/-}$ I-Tomcat Ai6 lungs. Sections were stained with SIRPα (dark blue), CD4 (yellow), Ai6 (green), and *Mtb*-expressed mCherry (magenta). White arrows indicate cells co-expressing Ai6 and SIRPα. (**C**) Image quantification of the frequency of Ai6 expression in CD4^{+} T cells and SIRPα^{+} IMs in the diseased and healthy tissue of B6 I-Tomcat Ai6 (n = 5) and *Sp140*$^{-/-}$ I-Tomcat Ai6 (n = 7) lungs. (**D**) Image quantification of the frequency of Ai6 expression among *Mtb*-infected macrophages or frequency of *Mtb* infection among Ai6^{+} cells for B6 I-Tomcat Ai6 (n = 5) and *Sp140*$^{-/-}$ I-Tomcat Ai6 (n = 7) lungs. All samples were analyzed 25 days after *Mtb* infection. Pooled data from two independent experiments are shown in (C) and (D). Statistical significance in (C) and (D) was calculated with an unpaired t test. ***$p < 0.001$.

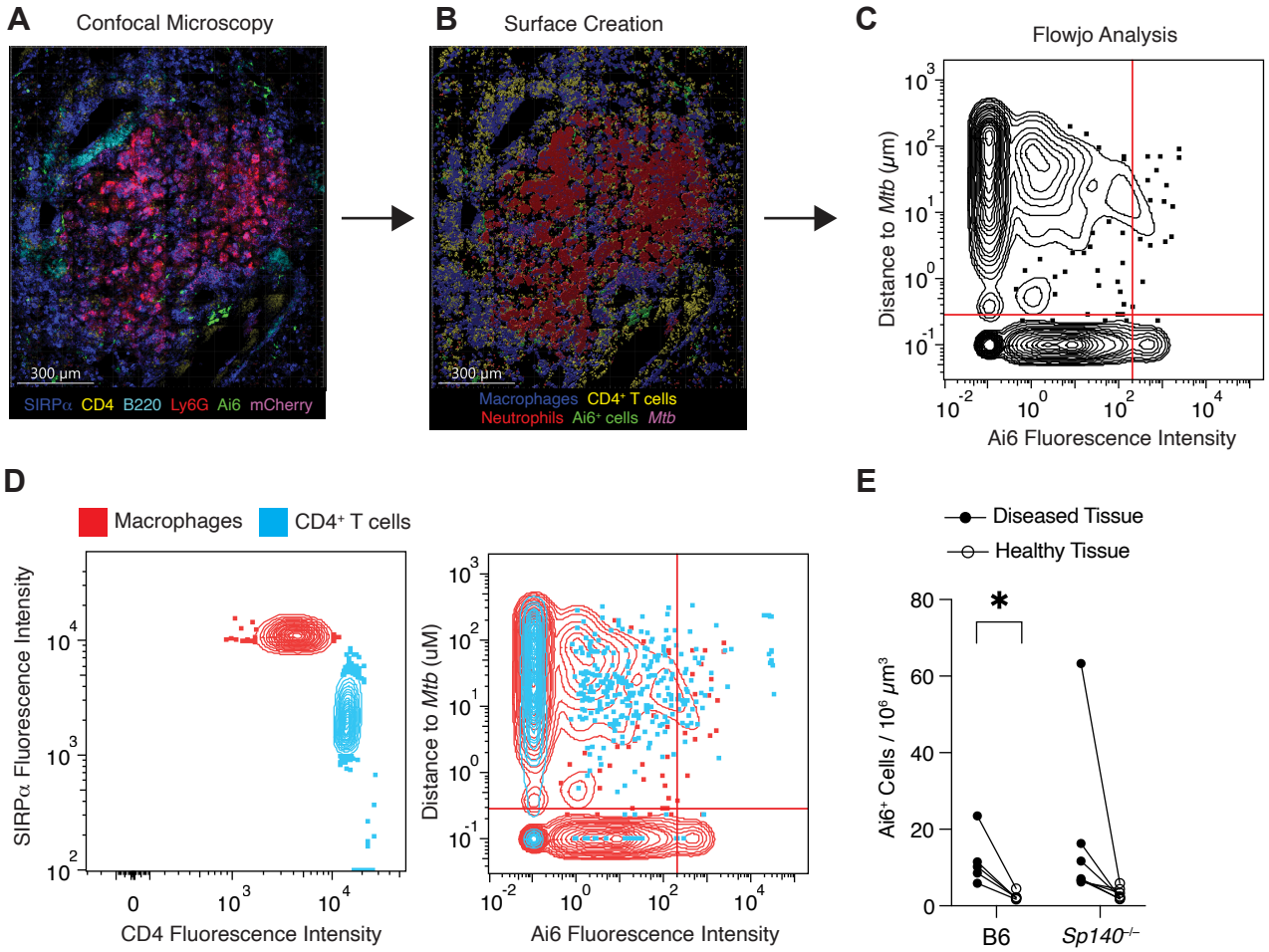

Supplementary Figure 7. Histo-cytometry image analysis of *Mtb*-infected I-Tomcat Ai6 mouse lungs. (**A**) Representative confocal microscopy image of SIRPα (dark blue), CD4 (yellow), B220 (teal), Ly6G (red), Ai6 (green), and mCherry (magenta) staining in a section of mouse lung 25 days after *Mtb* infection. (**B**) Identifying cells within the image based on fluorescence intensity of individual channels as well as cellular morphology. (**C**) Flowjo analysis to quantify fluorescent signal intensity and distance to *Mtb* for cells identified in the image. (**D**) Representative Flowjo comparison of macrophages (red) and CD4⁺ T cells (blue) from an image of a diseased portion of an *Sp140*$^{-/-}$ lung. (**E**) Number of Ai6⁺ cells per 10^6 um^3 in diseased (closed circle) and healthy tissue (open circle) from B6 (n = 5) and *Sp140*$^{-/-}$ (n = 7) *Mtb*-infected mouse lungs. Mouse lungs were harvested 25 days after infection. Pooled data from two independent experiments are shown in (E). Statistical significance in (E) was calculated by multiple paired t tests. *$p < 0.05$.

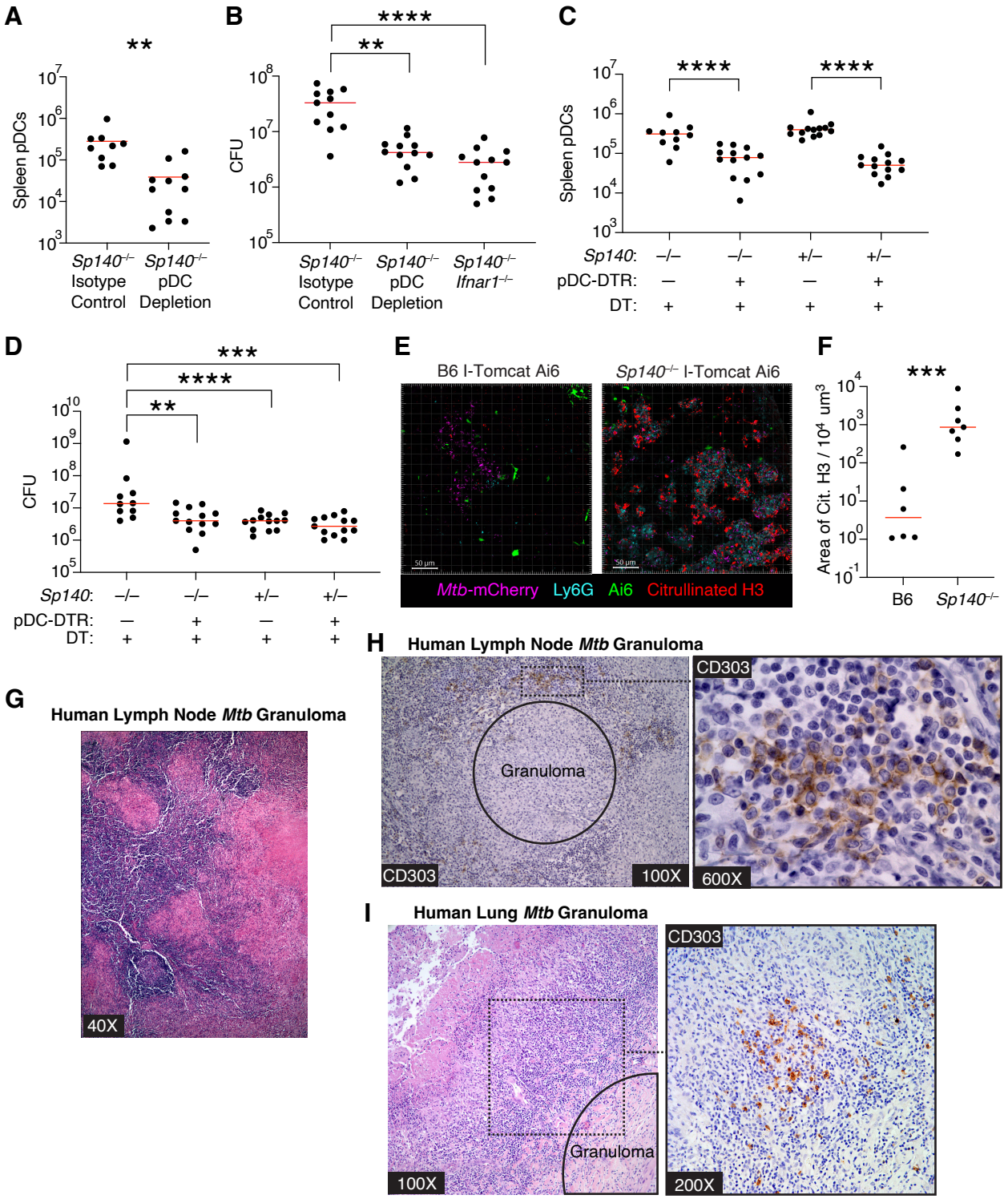

Figure 5. pDC depletion reduces *Mtb* burdens in *Sp140*$^{-/-}$ mice, and pDCs are present in the lymphocytic cuff surrounding granulomas in *Mtb*-infected human lymph nodes and lungs. (**A**) Number of splenic pDCs and (**B**) bacterial burden in *Sp140*$^{-/-}$ mice that received isotype or pDC depleting antibody from days 12 to 24 post-infection (n = 9-12). (**C**) Number of splenic pDCs and (**D**) bacterial burden in *Sp140*$^{-/-}$ pDC-DTR mice or *Sp140*$^{-/-}$ mice controls that received DT from days 12 to 24 after infection (n = 10-13). (**E**) Representative images and (**F**) quantification of NET production based on citrullinated H3 staining in the diseased portions of I-Tomcat Ai6 and *Sp140*$^{-/-}$ I-Tomcat Ai6 lungs. Sections were stained with citrullinated H3 (red), Ai6 (green), Ly6G (teal), and *Mtb*-expressed mCherry (magenta) (n = 6-7). (**G**) Representative hematoxylin and eosin or (**H**) anti-CD303 (brown) and hematoxylin staining on serial sections of *Mtb*-infected human lymph nodes (n = 8). (**I**) Representative hematoxylin and eosin and anti-CD303 (brown) and hematoxylin staining on serial sections of *Mtb*-infected human lung samples (n = 8). Mouse lungs were harvested 25 days post-infection. The bars in (A), (B), (C), (D), and (F) represent the median. Pooled data from two independent experiments are shown in (A), (B), (C), (D), and (F). Statistical significance was calculated by one-way ANOVA with Tukey's multiple comparison test for (B), (C), and (D) and by an unpaired t test for (A) and (F). **$p < 0.01$, ***$p < 0.001$, ****$p < 0.0001$.

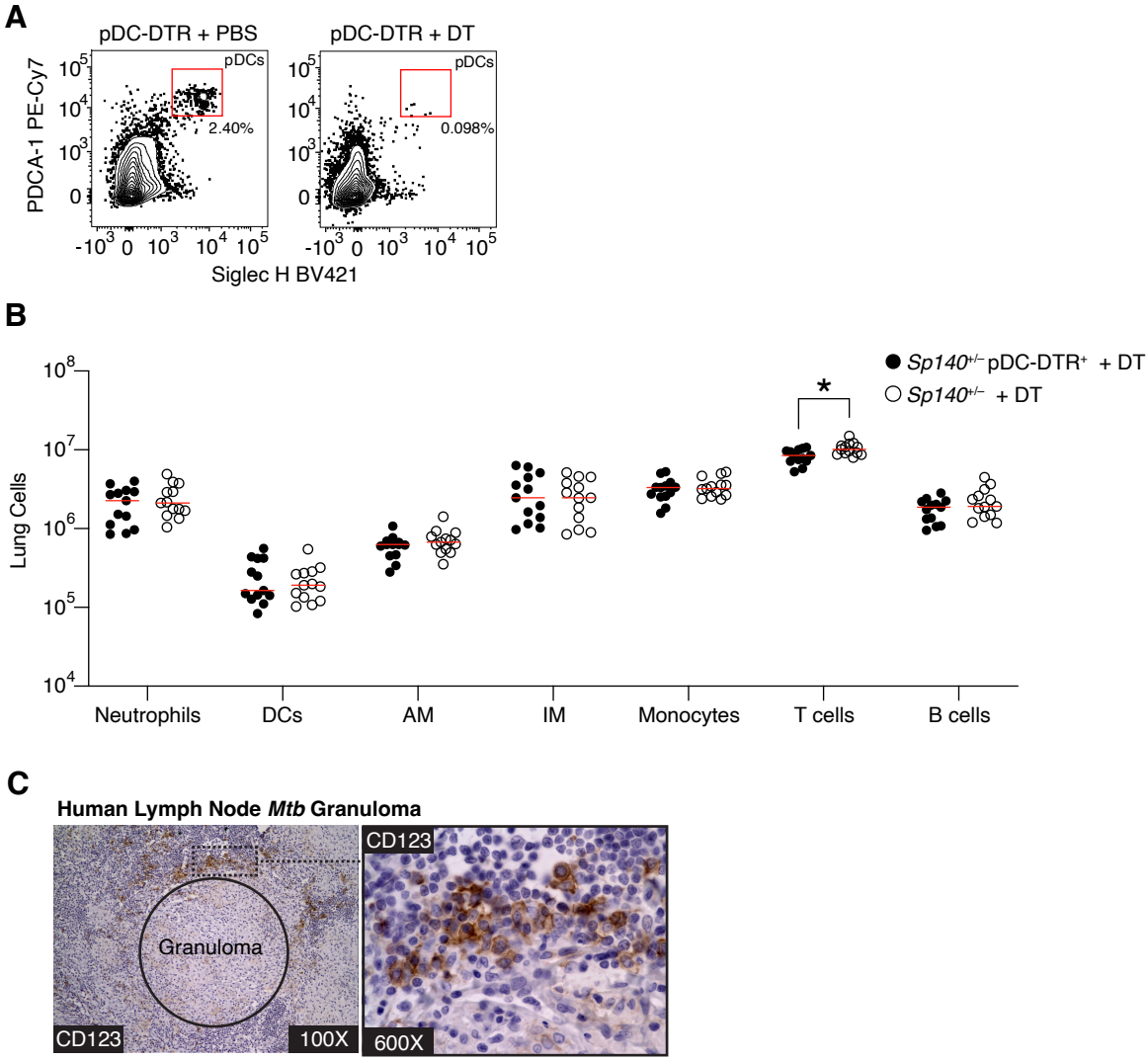

Supplementary Figure 8. pDC-DTR mice specifically deplete pDCs without affecting major lung immune cell populations, and CD123 also identifies pDCs in *Mtb*-infected human lymph node samples. (**A**) Representative flow cytometry plot of splenic pDCs in *Sp140*$^{+/-}$ pDC-DTR mice treated with PBS or DT from days 12 to 24 after *Mtb* infection. (**B**) Number of various immune cell populations in *Mtb*-infected lungs of *Sp140*$^{+/-}$ pDC-DTR (n = 13; filled circles) and *Sp140*$^{+/-}$ mice (n = 13; open circles). Mice received DT from days 12 to 24 post-infection. (**C**) anti-CD123 (brown) and hematoxylin staining on *Mtb*-infected human lymph nodes. Mouse lungs and spleens were harvested 25 days after infection. Pooled data from two independent experiments are shown in (B). The bars in (A), (B) represent the median. Statistical significance in (B) was calculated by multiple unpaired t tests. *$p < 0.05$.

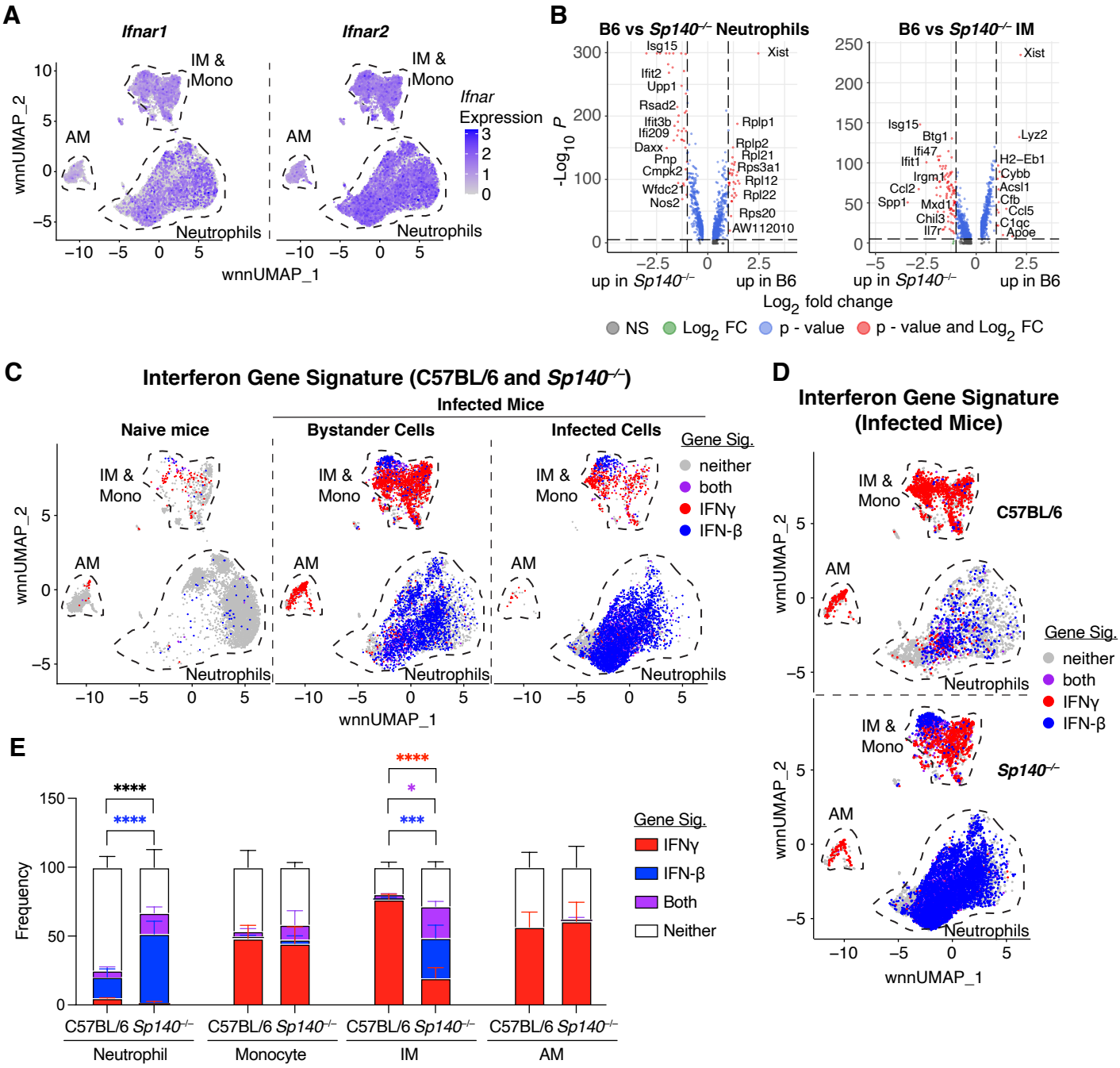

Figure 6. Neutrophils and IMs in *Mtb*-infected *Sp140*$^{-/-}$ lungs respond to type I IFNs and exhibit impaired responses to IFNγ. (**A**) Weighted nearest neighbor UMAP plot of *Ifnar1* and *Ifnar2* mRNA expression in innate immune cells from *Mtb*-infected lungs (B6 and *Sp140*$^{-/-}$ combined). (**B**) Volcano plot of differentially expressed genes comparing B6 and *Sp140*$^{-/-}$ neutrophils and IMs, with higher log fold change indicating greater expression in B6. (**C**) Weighted nearest neighbor UMAP plot of naïve, bystander, and *Mtb*-infected lung myeloid cells (B6 and *Sp140*$^{-/-}$ combined) classified by their responsiveness to IFNγ (red), type I IFN (blue), both (purple), or neither (grey). Signatures are defined in Supplementary Fig. 9A. (**D**) Weighted nearest neighbor UMAP plot and (**E**) graph of the frequency of neutrophils, monocytes, IMs, and AMs from bystander and *Mtb*-infected B6 (n = 3) and *Sp140*$^{-/-}$ (n = 3) lungs that are responsive to IFNγ (red), type I IFN (blue), both (purple), or neither (white). Lungs were analyzed 25 days after *Mtb*-Wasabi infection. Statistical significance in (B) was calculated with the Wilcoxon Rank-Sum test and by two-way ANOVA with Tukey's multiple comparisons test in (E). *$p < 0.05$, ***$p < 0.001$, ****$p < 0.0001$.

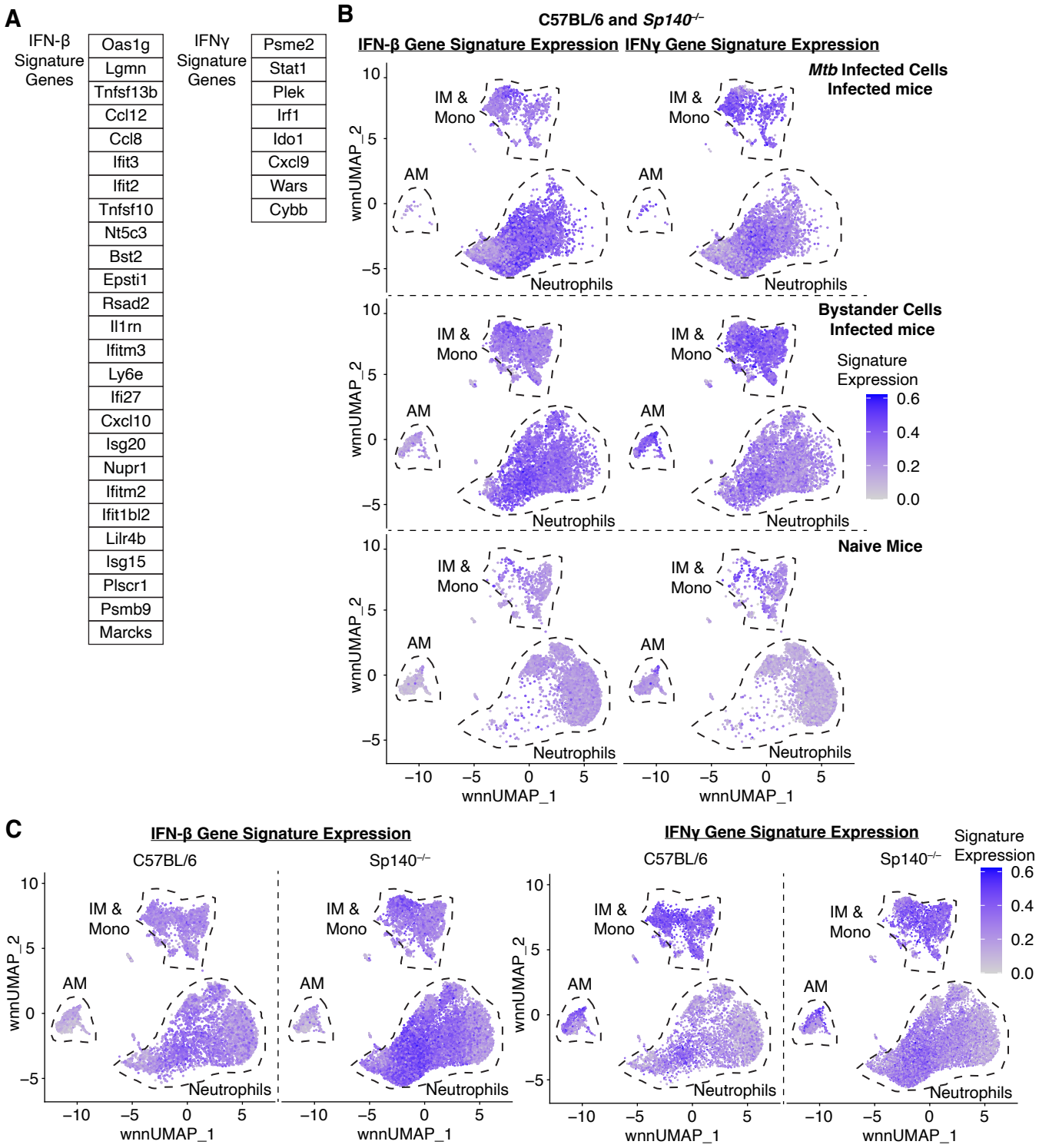

Supplementary Figure 9. Generating gene signatures for identifying IFNγ and type I IFN responding cells. (**A**) List of genes used for the gene signature for IFNγ or type I IFN responsiveness. (**B**) Weighted nearest neighbor UMAP plot of the IFNγ and type I IFN gene signature expression on naïve, bystander, or *Mtb*-infected lung myeloid cells (B6 and *Sp140*$^{-/-}$ combined). (**C**) Weighted nearest neighbor UMAP plot comparing IFNγ and type I IFN gene signature expression on cells from B6 and *Sp140*$^{-/-}$ lungs.

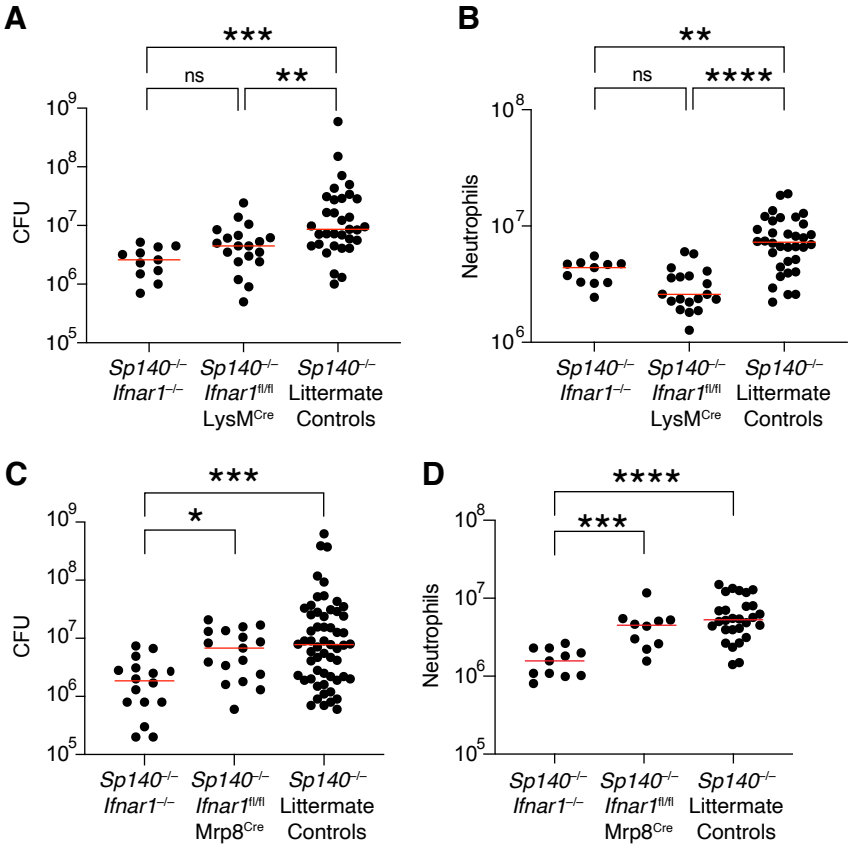

Figure 7. Macrophage recognition of type I IFN drives the *Mtb* susceptibility of *Sp140*$^{-/-}$ mice. (**A**) Colony forming units and (**B**) number of neutrophils in the lungs of *Sp140*$^{-/-}$ *Ifnar1*$^{-/-}$ (n = 11), *Sp140*$^{-/-}$ *Ifnar1*$^{fl/fl}$ LysM^{cre} (n = 18), and *Sp140*$^{-/-}$ littermate control (n = 34) mice 24-25 days after *Mtb* infection. (**C**) Bacterial burdens and (**D**) neutrophil numbers in the lungs of *Sp140*$^{-/-}$ *Ifnar1*$^{-/-}$ (n = 11-16), *Sp140*$^{-/-}$ *Ifnar1*$^{fl/fl}$ Mrp8^{cre} (n = 10-18), and *Sp140*$^{-/-}$ littermate control (n = 28-57) mice. The bars in (A), (B), (C), and (D) represent the median. Lungs were analyzed for the depicted experiments 24-26 days after *Mtb* infection. Pooled data from two-three independent experiments are shown. Statistical significance was calculated by one-way ANOVA with Tukey's multiple comparison test. *$p < 0.05$, **$p < 0.01$, ***$p < 0.001$, ****$p < 0.0001$.